Inductive Power Transfer based on Variable Compensation Capacitance to Achieve an EV Charging Profile with Constant Optimum Load

Grazian, Francesca; Soeiro, Thiago Batista; Bauer, Pavol

DOI
10.1109/JESTPE.2022.3188060

Publication date
2022

Document Version
Final published version

Published in
IEEE Journal of Emerging and Selected Topics in Power Electronics

Inductive Power Transfer Based on Variable Compensation Capacitance to Achieve an EV Charging Profile With Constant Optimum Load

Francesca Grazian, *Graduate Student Member, IEEE*, Thiago Batista Soeiro, *Senior Member, IEEE*, and Pavol Bauer, *Senior Member, IEEE*

***Abstract*— Wireless charging must be highly efficient throughout the entire battery charging profile to compete in the electric vehicle (EV) industry. Thus, optimum load matching is commonly used: it operates at the equivalent load that maximizes the efficiency, which depends on the coil's alignment. In this article, the optimum load is made independent of the coils' position by changing the system's resonant frequency through switch-controlled capacitors (SCCs). This eliminates the need for load-side voltage control. The output current follows the battery voltage rise during the battery charging cycle to always match the optimum load, which can be achieved by regulating the input voltage via the power factor correction (PFC) converter. This method is called here constant optimum load (COL). Two SCC topologies have been implemented in a 3.7-kW hardware demonstrator. The one implementing the half-wave modulation achieves higher efficiency than the one employing full-wave modulation, with 96.30% at 3.2 kW and aligned coils. When misalignment occurs, the half-wave modulation technique results in higher efficiency than the conventional-fixed compensation, where the efficiency is lower by up to 0.68% at partial load. Based on these results, the proposed COL method is proven suitable for 3.7-kW EV-static wireless charging achieving one of the highest peak efficiencies listed in today's literature for the same power class.**

***Index Terms*— Compensation networks, control, inductive power transfer (IPT), magnetic resonant coupling, optimum load matching, soft switching, switch-controlled capacitors (SCCs), wireless charging, zero voltage switching (ZVS).**

I. Introduction

THE industry of electric vehicles (EVs) for private use is predicted to grow exponentially in the next decade. According to [1], wireless charging has the potential of increasing the users' interest in EVs if this option would be included. This means that wireless charging can play a key role in the driver decision to buy an EV.

Manuscript received 7 March 2022; revised 3 May 2022; accepted 20 June 2022. Date of publication 4 July 2022; date of current version 3 February 2023. This work was supported by the Delft University of Technology (TU Delft), Electrical Sustainable Energy Department. Recommended for publication by Associate Editor Minjie Chen. *(Corresponding author: Francesca Grazian.)*

The authors are with the Electrical Sustainable Energy Department, Delft University of Technology, 2628 CD Delft, The Netherlands

Color versions of one or more figures in this article are available at https://doi.org/10.1109/JESTPE.2022.3188060.

Digital Object Identifier 10.1109/JESTPE.2022.3188060

EV wireless charging is most commonly realized through inductive power transfer (IPT) with magnetic resonance [2], [3]. For instance, a transmitting coil transfers power to a receiving coil via a time-varying magnetic field. These coupled coils constitute an intrinsically isolated resonant converter.

EV wireless charging can be implemented as static, quasi-dynamic, or dynamic charging, depending on the relative position of the receiving coil with respect to the transmitting coil as a function of the time [4]. For instance, in the case of static charging, the distance between the magnetic centers of the coils is fixed during one charging cycle, while in the case of dynamic charging, it continuously changes. Quasi-dynamic charging has both characteristics during one charging cycle.

The static EV wireless charging aims to substitute or complement the traditional EV charging through cable because of its user convenience, which becomes fundamental in the case of autonomously driven cars. Although, the true advantage of static EV wireless over cable charging must be supported by an efficient power transfer at different operating conditions. This would translate into a relatively low demand of input energy for each charging cycle, which is essential for realizing a sustainable and cost-effective EV charging solution. The high power transfer efficiency of an EV wireless charging system must be accounted for when designing the system and during the charging operation.

In the design stage, the optimized charging coils' structure has been widely investigated, since they contribute to a considerable part of power losses. In [6]–[10], multiobjective optimizations of the coils have been performed. The optimization of the cores' structures using artificial intelligence (AI) has been explored in [11]. Advancements in magnetic materials have been researched in [12]. To reduce the drop in magnetic coupling with the misalignment, multicoils configurations have been compared with the single-coil ones in [9]. For what concerns the power converters, wireless charging systems differ in the number of power conversion stages, as summarized in [13], which depend on the implemented control strategy.

During the charging process, it is fundamental that the maximization of the power transfer efficiency is achieved while the control strategy follows the conventional EV battery charging

profile that consists of the constant current (CC) and the constant voltage (CV) modes. For this purpose, the optimum load impedance matching defined in [6] and [14] has been widely adopted [9], [15]–[22]. This strategy sets the operation at the equivalent load that maximizes the efficiency, i.e., optimum load, which depends on the coils' alignment. The latter is realized for a large variation of the magnetic coupling via voltage control at load side, which, in [15] and [17]–[19], uses a post-regulating dc/dc converter. At the same time, the input voltage is regulated to supply the output current required for the CC and CV operations. For that purpose, [9] and [19] use a boost-type power factor correction (PFC) rectifier, while [15] and [18] use an additional dc/dc converter. Undoubtedly, those auxiliary power converter stages introduce extra losses that would worsen the overall efficiency of the system in some operating range. Since the battery voltage increases during one charging cycle, the voltage regulation at both the input and output must always be active. Consequently, the losses introduced by these converters might be considerable when accounting for the entire charging process. On the other hand, [16] performs the optimum load matching through phase shift modulation of the primary and secondary bridges of the resonant converter. However, the switching losses become considerable in some operating conditions. To achieve the zero voltage switching (ZVS) in the whole operating range, [21] uses asymmetrical phase shift modulation of the two converter's bridges. Moreover, the circulating reactive power is minimized by utilizing switch-controlled capacitors (SCCs) as compensation. A flat efficiency is achieved for a wide output power range, but the resulting efficiency is not shown when the coil misalignment occurs. In addition, [22] uses a semi-active rectifier to match the optimum load as the load varies. At the same time, the amount of reactive power is controlled by employing a SCC as secondary compensation capacitance. Thereby, the input voltage is not controlled, since minor variations of the coupling factor are considered.

Besides [21] and [22], SCCs have been used in other IPT systems. For instance, they have been utilized to match the resonant frequency with the selected constant operating frequency, as the self-inductance of the coils changes in the presence of misalignment [23]–[26]. In addition, SCCs have been employed as part of IPT systems with high-order compensation networks, such as the double-sided LCC (LCC-LCC) and the LCC-series (LCC-S), to control the output power [27]–[29]. However, all these papers consider relatively low power levels ($\leq$500 W). Therefore, the SCC applicability to IPT systems with power levels typical of EV charging has not been proved yet. This might be critical, especially due to the high voltage stress that characterizes the compensation capacitors, translating into the high required blocking voltage from the SCC semiconductors. The requirement for relatively high blocking voltage semiconductors is critical for mainly two reasons. First, the typical static losses are larger than in the lower voltage classes [30], and possibly, the supply chain is limited for higher blocking voltages, e.g., $>$1200 V.

This article explains and proves experimentally an efficiency enhancement strategy for EV wireless charging, which consists of making the optimum load invariant of the coils' alignments as preliminary explained in [31]. This method is named here as constant optimum load (COL) charging. The optimum load is maintained constant at different coils' alignments by varying the system's resonant and operating frequency. The latter is realized by employing a series-connected SCC to compensate both the primary and secondary coils. The key advantage is that there is no need for voltage control on the load side. During the charging process, only the input voltage is regulated to vary the output current, as the battery voltage increases to realize a constant equivalent resistive load at the output. This takes the name of COL charging, which substitutes the conventional CC mode.

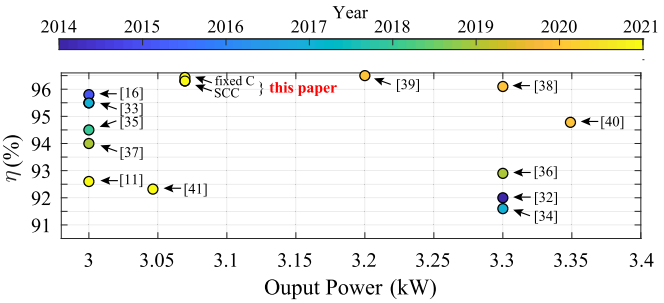

Fig. 1. Measured peak dc-to-dc efficiency η of this article compared with the available literature with the same J2954-based EV charger power class (WPT1 = 3.7-kVA maximum input [5]).

For the selected power level of 3.7 kW and with reference to Fig. 1, it is worth mentioning that in this article, the designed IPT system reached a measured peak efficiency of 96.30%, which is remarkably high with respect to the available literature [11], [16], [32]–[41]. In Fig. 1, the losses of the necessary PFC rectifier are not included, since they would be present in all the IPT systems. According to the power losses analysis in Section IV-B, the measured peak efficiency could be increased to 96.77% just by substituting the diodes in the H-bridge rectifier stage with the same SiC MOSFETs employed in the inverter stage operating in synchronous rectification.

The original contributions of this article are as follows.

1) Prove that the proposed COL charging method can be achieved through SCCs and the PFC rectifier for a range of magnetic coupling and battery voltage, which is typical or static EV wireless charging while respecting the standardized operating frequency range 79–90 kHz.
2) Detailed analytical modeling, implementation, and comparison in terms of efficiency of two different SCCs for EV wireless charging, where one implements the full-wave modulation and the other uses the half-wave modulation.
3) Benchmark of the proposed COL charging with SCCs against the conventional CC mode with fixed compensation capacitors where the primary coil current distortion is also analyzed.

The remaining sections of this article are organized as follows. The analytical modeling and the overall process of the proposed COL method are explained in Section II, while the implementation is discussed in Section III, resulting in the design of a 3.7-kW laboratory prototype. The experimental results are illustrated and discussed in Section IV.

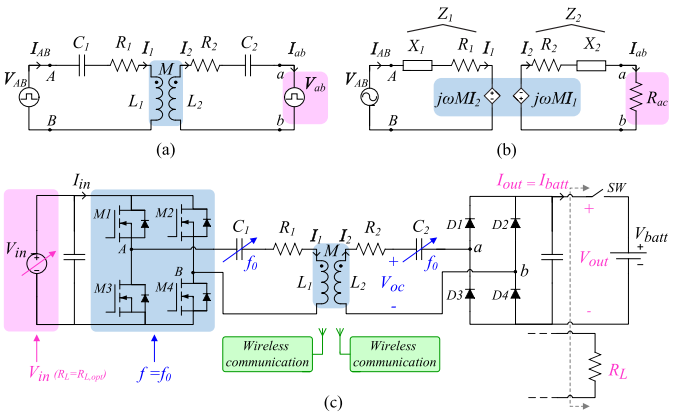

Fig. 2. Equivalent circuits of the S–S compensation network. Simplified high-frequency circuits based on (a) realistic IPT system and (b) equivalent circuit where M is modeled as a current-controlled voltage source and the load is depicted as the equivalent first-harmonic resistance $R_{\rm ac}$. (c) Implementation of the proposed COL charging method whose concept is shown in Fig. 5.

Finally, the main conclusions on this research are drawn in Section V.

II. Variable Compensation Capacitance for Operation With COL

A. Analytical Concept for Different Coils' Mutual Inductance

The equivalent circuit of an EV wireless charging system that uses the S–S compensation network is shown in Fig. 2. Thereby, L_1 is the primary coil self-inductance, and L_2 is the coil secondary self-inductance of which the magnetic coupling $k = (M/(L_1L_2)^{1/2})$ depends on the coils' mutual inductance M. Moreover, C_1 and C_2 are the S–S network's compensation capacitances, and R_1 and R_2 are the lumped series resistances modeling the losses of the primary and the secondary circuits' components. The currents flowing through the primary and secondary circuits are $\boldsymbol{I_{AB}} = \boldsymbol{I_1}$ and $\boldsymbol{I_{ab}} = \boldsymbol{I_2}$, respectively. To match a more realistic configuration of an IPT system, Fig. 2(a) represents both the input supply $\boldsymbol{V}_{AB}$ and the output load $\boldsymbol{V}_{ab}$ as square-wave voltage sources. On the other hand, Fig. 2(b) shows a further simplified equivalent circuit well useful to verify the performance of the circuit in a single static operating point in which all voltages and currents are assumed to be sinusoidal waveforms with the fundamental frequency of $\boldsymbol{V}_{AB}$. In this case, the influence of M is represented as current-controlled voltage sources, and the load is depicted as the equivalent resistance $R_{\rm ac}$. It must be pointed out that M and $R_{\rm ac}$ are likely to vary in IPT systems, because the coils' position is not fixed, and the voltage of lithium-ion batteries changes during the charging process, as the battery's state-of-charge (SoC) varies.

For a given operation, the voltages and currents of the circuit in Fig. 2(b) can be found from the Kirchhoff voltage law in (1), where $\boldsymbol{V_{AB}}$ is taken as a reference, such that, according to the phasor convention, $\boldsymbol{V_{AB}} = \hat{V}_{AB}\angle 0°$. According to [42], $\hat{V}_{AB}$ and $R_{\rm ac}$ are defined in (2) and (3) based on the fundamental component of $\boldsymbol{V_{AB}}$, $\boldsymbol{V_{ab}}$, and $\boldsymbol{I_2}$. Furthermore, the primary and secondary impedances $\boldsymbol{Z_1}$ and $\boldsymbol{Z_2}$ are defined in (4)

$$\begin{cases} \boldsymbol{V_{AB}} = \boldsymbol{Z_1 I_1} + j\omega M \boldsymbol{I_2} \\ 0 = (\boldsymbol{Z_2} + R_{\rm ac})\boldsymbol{I_2} + j\omega M \boldsymbol{I_1} \end{cases} \tag{1}$$

$$\hat{V}_{AB} = \frac{4}{\pi} V_{\rm in} \tag{2}$$

$$R_{\rm ac} = \frac{\boldsymbol{V_{ab}}}{\boldsymbol{I_2}} \approx \frac{8}{\pi^2} R_L \tag{3}$$

$$\boldsymbol{Z_1} = R_1 + j\omega X_1, \quad X_1 = \omega L_1 - \frac{1}{\omega C_1}$$

$$\boldsymbol{Z_2} = R_2 + j\omega X_2, \quad X_2 = \omega L_2 - \frac{1}{\omega C_2}. \tag{4}$$

One of the main challenges in IPT systems used in charging applications is to achieve a highly efficient power transfer at different operating conditions. From (1), the power transfer efficiency $\eta_{\rm ac}$ results in (5). The latter is maximized when $R_{\rm ac}$ is equal to the optimum load $R_{\rm ac,opt}$ in (6)

$$\eta_{\rm ac} = \frac{R_{\rm ac}|\boldsymbol{I_{ab}}|^2}{V_{AB}\,\mathrm{Re}[\boldsymbol{I_{AB}}]} = \frac{\frac{R_{\rm ac}(\omega M)^2}{|(R_{\rm ac}+Z_2)Z_1+(\omega M)^2|^2}}{\mathrm{Re}\left[\frac{Z_2+R_{\rm ac}}{(R_{\rm ac}+Z_2)Z_1+(\omega M)^2}\right]} \tag{5}$$

$$R_{\rm ac,opt} = \underbrace{R_2\sqrt{\frac{(\omega_0 M)^2}{R_2R_1}+1}}_{\frac{d}{dR_{\rm ac}}(\eta_{\rm ac})|_{\omega=\omega_0}=0} \overset{\frac{(\omega_0 M)^2}{R_2R_1}\gg 1}{\approx} \underbrace{\omega_0 M\sqrt{\frac{R_2}{R_1}}}_{\frac{d}{dR_{\rm ac}}\left(\frac{R_1I_1^2+R_2I_2^2}{R_{\rm ac}I_{ab}^2}\right)|_{\omega=\omega_0}=0}. \tag{6}$$

Moreover, if $(\omega_0 M)^2 \gg R_2R_1$ is valid, $R_{\rm ac,opt}$ corresponds to the equivalent load that minimizes the sum of the primary and secondary circuits' conduction losses with respect to the output power as defined in [9]. When R_1 and R_2 are the lump equivalent series resistances modeling the losses of the whole circuit (semiconductors, compensation capacitor, and coil), $R_{\rm ac,opt}$ maximizes the efficiency of the entire system. The respective $R_{L,\rm opt}$ is found by substituting (6) into (3).

According to (6), the value of $R_{\rm ac,opt}$ depends on the angular resonant frequency ω_0, the coils' mutual inductance M, and the lump resistances R_1 and R_2. When the coils' position varies, the condition on $R_{\rm ac,opt}$ is not fixed, and it is directly proportional to M. Furthermore, during the CC and CV battery charging modes, the equivalent resistive load R_L varies continuously, meaning that the condition $R_L = R_{L,\rm opt}$ would be met only in one operating point. An example of this is illustrated in the battery charging profile in Fig. 3(a), which shows that it is not possible to match the optimum load operation $R_L = R_{L,\rm opt}$ at all times without employing voltage control at the secondary circuit. In [6], the secondary voltage control is performed by a post-regulating dc–dc converter, which might add substantial losses to the circuit. Alternatively, [16] and [21] control the output voltage by phase shifting the rectifier stage composed of active semiconductors. Moreover, the target output power according to the CC and CV charging modes can be set by controlling the input voltage through a pre-regulator circuit, which can be the necessary ac grid-connected PFC circuit or another non-isolated dc/dc converter.

Fig. 4 shows the examples of $V_{\rm in}$ and $V_{\rm out}$ ranges required to achieve optimum load matching during the CC charging mode

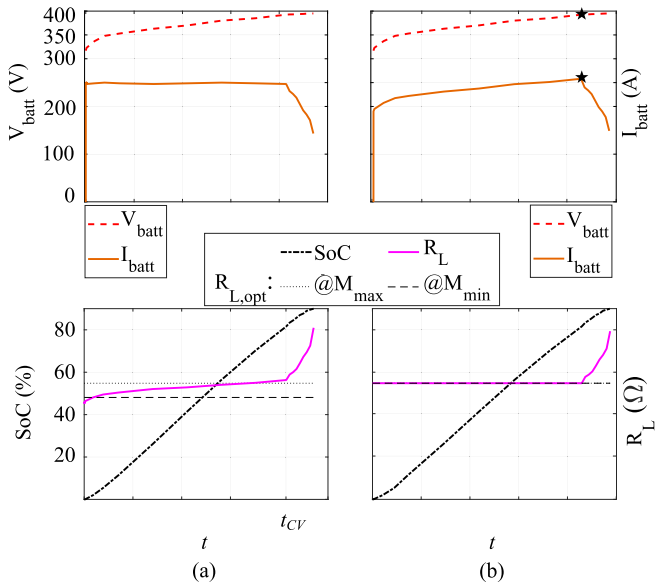

Fig. 3. Battery charging profile that uses (a) traditional CC method and (b) proposed COL method. This example is based on one measured charging cycle of a Nissan Leaf's battery [43]. Top plots: battery voltage V_{batt} and current I_{batt}. Bottom plots: battery state of charge or SoC, the equivalent load resistance R_L and the optimum load $R_{L,\text{opt}}$ at both the minimum M_{min} and maximum M_{max} mutual inductance values.

in Fig. 3(a) for different M values. The power classes defined by SAE J2954 have been chosen where the specified power level is the maximum allowed from the ac grid connection. Among these, 22 kW is currently under consideration [5]. The power classes in Fig. 4(a) use the one-phase (1-ϕ) connection to the European low-voltage 50-Hz grid, while a 3-ϕ grid connection is considered for the power classes in Fig. 4(b). This choice is due of the fact that households in Europe have limited access to grid connections with more than 16 A for each 230-V phase. This analysis assumes that $\boldsymbol{Z_1} = \boldsymbol{Z_2} = 0$ when operating at $\omega = \omega_0$, and M is computed from

$$I_{\text{out}} \approx \frac{2}{\pi}\hat{I}_{ab} \approx \frac{8}{\pi^2}\frac{V_{\text{in}}}{\omega_0 M}. \tag{7}$$

In all power classes, the input and output voltages need to be continuously controlled to achieve the optimum load matching at different M values while following the CC charging mode.

Instead of varying R_L to always match the M-dependent $R_{L,\text{opt}}$, this article proposes to keep the value of $R_{L,\text{opt}}$ constant over different M values by varying the system's resonant frequency $f_0 = (\omega_0/2\pi)$, as qualitatively shown in Fig. 5. This strategy defines the COL operation. According to (6), this is possible, since $R_{\text{ac,opt}}$ is directly proportional to both M and ω_0. The proposed battery charging profile is shown in Fig. 3(b). For most of the charging cycle and for the whole range of $M = [M_{\text{min}}\ M_{\text{max}}]$, R_L is equal to $R_{L,\text{opt}}$, which ensures maximum power transfer efficiency. The proposed COL charging only requires input voltage control, as shown in Fig. 4. The main advantage is that there is no need for voltage control at the secondary circuit to satisfy $R_L = R_{L,\text{opt}}$. This can eliminate one power conversion stage, and consequently, it allows power loss reduction. It must be noted that standards for static EV wireless charging applications [5], [44] constrain the range of the H-bridge inverter operating frequency between 79 and 90 kHz limiting the M range covered by the COL implementation, as considered in Fig. 4. However, Sections III and IV will show that the proposed COL concept with the usage of SCCs can be well exploited in the frequency range established by these standards within the charging cycle and misalignment range typical of commercial EVs.

B. Proposed COL Process for the Battery Charging Cycle

The circuit of the proposed COL method is shown in Fig. 2(c). The process is summarized in the flowchart of Fig. 6.

1) Before the Start of the Power Transfer: The process starts with the measurement of the coils' mutual inductance M explained in Section III-A. Based on the value of M, the system's resonant frequency $f_0 = \omega_0/2\pi$ that keeps $R_{L,\text{opt}}$ constant to the value at perfect alignment can be calculated from (3) and (6). Then, the resulting f_0 can be set by employing one variable compensation capacitor at both the primary and secondary circuits.

In (4), the value of C_2 must be selected, such that i_2 is slightly capacitive with respect to v_{ab} at $f = f_0$ to reduce losses due to the reverse recovery (RR) of the rectifier's diodes. At the same time, the reactive power circulating in the secondary circuit must be minimized. This can be achieved by selecting

$$X_2 = R_{\text{ac}} \cdot \tan\left[\sin^{-1}\left(\frac{I_{\text{RR}}}{\hat{I}_2}\right)\right]. \tag{8}$$

On the other hand, C_1 must be tuned at $f = f_0$, such that the inverted current i_1 would lag the inverted voltage v_{AB}, which makes the primary inverter achieving ZVS turn-on. As explained in [45], to minimize the reactive power in the primary circuit, the inverter's turn-off current I_{OFF} must be close to the minimum value given in 9 that ensures ZVS turn-on of the opposite leg by completely discharging the MOSFETs' drain–source capacitance C_{ds} during the dead time t_{dead}

$$I_{\text{OFF,min}} \approx \frac{2 \cdot C_{\text{ds}} \cdot V_{\text{in,max}}}{t_{\text{dead}}}. \tag{9}$$

Therefore

$$X_1 = R_{\text{in}} \cdot \tan\left[\sin^{-1}\left(\frac{I_{\text{OFF}}}{\hat{I}_1}\right)\right] \tag{10}$$

where R_{in} is the real part of the input impedance $\boldsymbol{Z}_{\text{in}}$ in (11), which is seen from the source V_{AB} at $f = f_0$. In (11), X_2 has been neglected, since it is assumed that $R_{\text{ac}} \gg X_2$. The step-by-step computation of (10) is explained in Appendix A

$$\boldsymbol{Z}_{\text{in}} = \underbrace{R_1 + \frac{(\omega_0 M)^2}{R_2 + R_{\text{ac}}}}_{R_{\text{in}}} + j\underbrace{\left(\omega_0 L_1 - \frac{1}{\omega_0 C_1}\right)}_{X_{\text{in}} = X_1}. \tag{11}$$

The resulting C_1 and C_2 can be found from (12). After that, the inverter's operating frequency is set at $f \approx f_0$

$$C_1 = \frac{1}{(\omega_0 L_1 - X_1)\omega_0}, \quad C_2 = \frac{1}{(\omega_0 L_2 - X_2)\omega_0}. \tag{12}$$

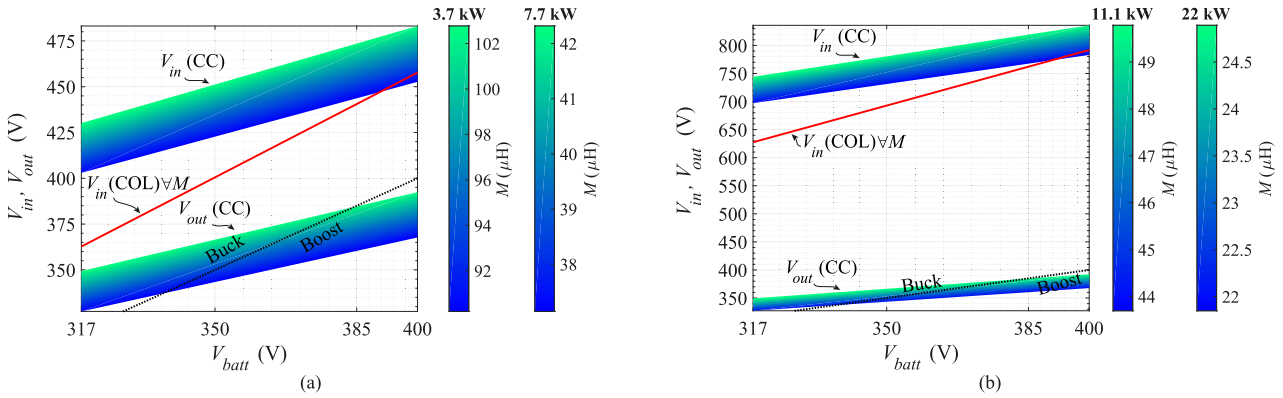

Fig. 4. Required dc voltages V_{in} and V_{out} from the CC charging and the proposed COL charging methods depending on M for a complete charging cycle of a 400-V EV battery. Example for the power levels of (a) 3.7 kW ($I_{\text{batt}} = 7$ A, $t_{CV} = 8.1$ h) and 7.7 kW ($I_{\text{batt}} = 17$ A, $t_{CV} = 3.4$ h) and (b) 11.1 kW ($I_{\text{batt}} = 25$ A, $t_{CV} = 2.3$ h) and 22 kW ($I_{\text{batt}} = 50$ A, $t_{CV} = 1.2$ h). The values of I_{batt} and t_{CV} are defined based on the battery charging profile in Fig. 3(a).

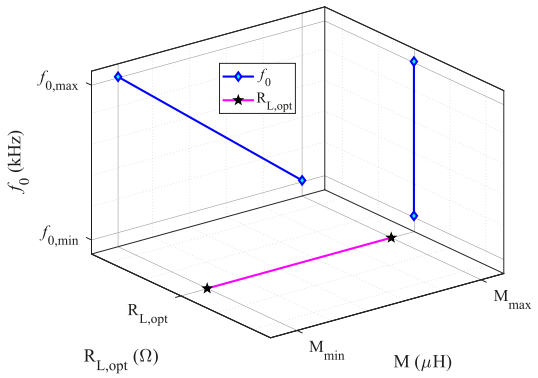

Fig. 5. Qualitative representation of the proposed COL method over different coils' alignments: the resonant frequency f_0 is varied to keep the optimum load $R_{L,\text{opt}}$ fixed over different coils' mutual inductances M. The frequency range from $f_{0,\min}$ to $f_{0,\max}$ must be within the standardized range 79–90 kHz established for the switching frequency of the IPT inverter bridge.

In static wireless charging applications, M stays the same during one charging cycle. Therefore, the measurement of M and the selection of f_0, C_1, and C_2 must be performed only once before starting of a new power transfer.

The initial battery voltage V_{out,t_0} is measured and communicated to the primary circuit. The input voltage V_{in,t_0} is regulated according to (7), such that the output current I_{out} would generate $R_L = R_{L,\text{opt}} = (V_{\text{out},t_0}/I_{\text{out}})$. The control of V_{in} is executed through a boost-type PFC rectifier, which can be implemented as explained in [46] and [47]. At this point, the power transfer is started.

2) During the Power Transfer: The value of R_L is continuously monitored, such that V_{in} can be adjusted to keep $R_L = R_{L,\text{opt}}$, while V_{out} increases. R_L can be computed by measuring the dc output components for the voltage and current, V_{out} and I_{out}. This is easier to implement than the direct monitoring of R_{ac} deriving from the high-frequency output variables. Assuming that the diodes are in a continuous conduction mode and that the operating frequency is close to the resonant frequency of the secondary circuit, R_{ac} can be derived from (3). The proposed COL strategy results in the battery charging profile shown in Fig. 3(b).

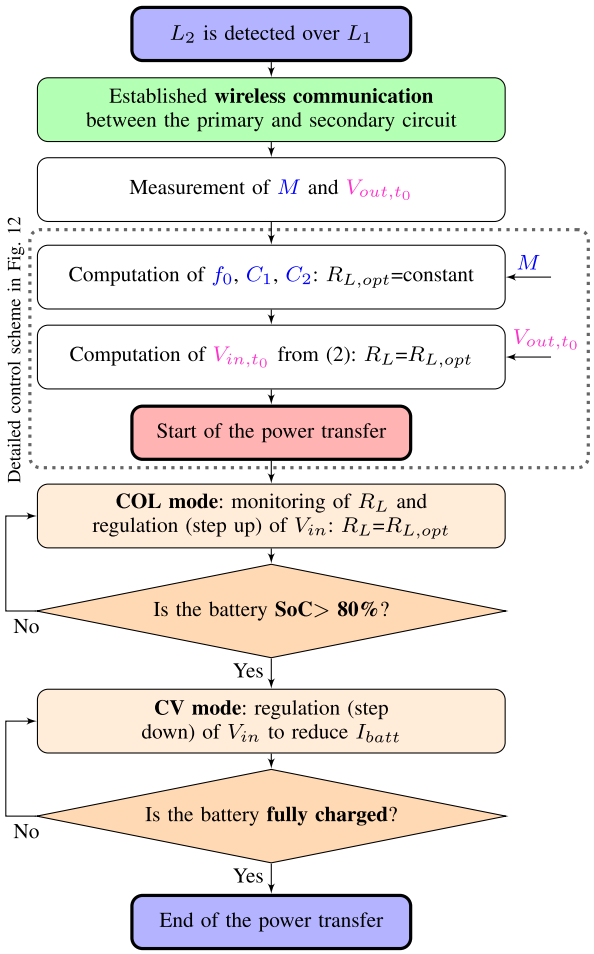

Fig. 6. Flowchart of the charging process proposed in Section II-B.

For the considered Nissan Leaf battery [43], the SoC reaches 80% of the full charge, and the standard CV charging phase starts. In particular, I_{batt} is gradually reduced by lowering V_{in} through the PFC. This last CV charging phase would eventually not operate at the maximum efficiency, but this is acceptable, since this time interval only contributes to the last 10% increase of the battery SoC, and according to Fig. 3, it has a much shorter duration and lower power processing than the COL mode.

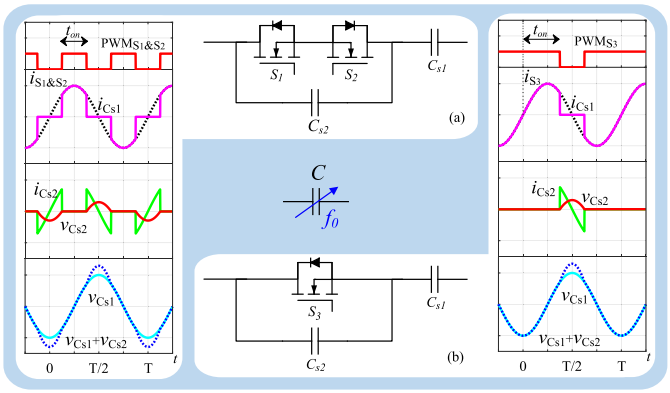

Fig. 7. Implementation of variable compensation capacitors as SCC with (a) full-wave and (b) half-wave modulations, where the equivalent capacitance results in (15) and (16), respectively.

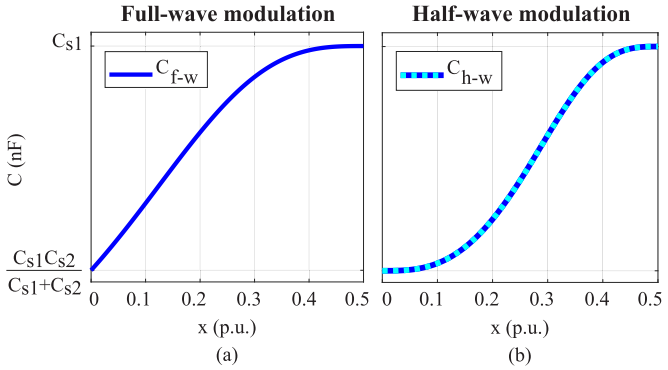

Fig. 8. Compensation capacitance C_{f-w} and C_{h-w} depending on $x = (t_{ON}/T)$ where the SCC uses (a) full-wave and (b) half-wave modulations.

III. Implementation

The functionality and the advantages of the wireless charging scheme proposed in Section II must be proved experimentally. Hereby, the implementation of such system is explained.

A. Mutual Inductance Measurement

Once the secondary coil has been detected by the primary circuit, the coil's mutual inductance M can be estimated, as shown in (13). This is valid by assuming that the battery is disconnected from the rest of the circuit, which is possible through the mechanical switch SW in Fig. 2(c)

$$M = \frac{V_{oc}}{\omega_0 I_1}. \tag{13}$$

Since the system operates at $f = f_0$ by varying the value of C_1, there is no need for measuring the phase angle of V_{oc} and I_1.

B. Variable Compensation Capacitor

The variable compensation capacitors of both the primary and the secondary circuits in Fig. 2(c) are implemented as the SCCs illustrated in Fig. 7. The SCC was first introduced by [48] to regulate resonant converters instead of varying the switching frequency. According to [48], the SCC has two possible implementations depending on the control strategy chosen for the semiconductor switches, which, for the chosen application, are SiC MOSFETs. When the SCC is switched on and off twice during one switching cycle, the control takes the name of full-wave modulation. The typical operating waveform and the switch arrangement are shown in Fig. 7(a). On the other hand, Fig. 7(b) shows another possible control strategy called half-wave modulation, where the SCC is switched on and off only once during one switching cycle. Hereby, the series-connected SCC has been selected to limit the maximum voltage stress on the MOSFETs, which is going to be discussed in Section III-D. Both modulations have the control signal synchronized with the current $i_{C_{s1}}$ flowing through the SCC series capacitor C_{s1}. Once the MOSFETs are turned off, that current would start flowing through C_{s2}. At that moment, the voltage across C_{s2} starts rising reaching the maximum when the current equals zero. After that, the current through C_{s2} would assume the opposite sign causing the decrease of $v_{C_{s2}}$. Once $v_{C_{s2}}$ approaches the zero, the MOSFETs are turned on again. This operation guarantees the ZVS of the SCCs.

Intuitively, the highest equivalent series capacitance is achieved when the semiconductor switches are always conducting, while the capacitance would be minimum if they are always blocking. Therefore, the equivalent capacitance $C_{s2,eq}$ depends on the on-time t_{ON} of the switches, which can be found from (14) by computing the fundamental component's amplitude of the voltage $v_{C_{s2}}$. This results in (15) for the full-wave modulation and in (16) for the half-wave modulation, where x is the duty cycle $x = (t_{ON}/T) = [0, \ldots, 0.5]$.

The capacitance variation of both C_{f-w} and C_{h-w} is shown in Fig. 8 as a function of x. In Section IV, the performance of both implementations is evaluated and compared with respect to the proposed COL battery charging method

$$\left(\hat{V}_{C_{s2}}\right)_1 = \frac{2}{T}\int_0^T v_{C_{s2}}(t)\cdot\cos\left(\frac{2\pi}{T}t\right)dt = -\frac{\hat{I}_{C_{s1}}}{\omega}\frac{1}{C_{s2,eq}} \tag{14}$$

$$C_{f-w} = \frac{1}{\frac{1}{C_{s1}} + \frac{1}{C_{s2,eq}}} = \frac{1}{\frac{1}{C_{s1}} + \frac{1}{C_{s2}}\left(\frac{\pi - 2\pi x - \sin 2\pi x}{\pi}\right)} \tag{15}$$

$$C_{h-w} = \frac{1}{\frac{1}{C_{s1}} + \frac{1}{C_{s2,eq}}} = \frac{1}{\frac{1}{C_{s1}} + \frac{1}{C_{s2}}\left(\frac{2\pi - 4\pi x + \sin 4\pi x}{2\pi}\right)}. \tag{16}$$

Besides the capacitance variation with respect to the duty cycle x, it is interesting to model the losses of the SCC.

The switching losses of the SCC can be considered negligible if the ZVS operation is achieved.

The conduction losses directly depend on x, since it defines the current conduction path within the SCC. The equivalent resistance of the SCC is described by (17) and (18) for the full-wave and the half-wave modulations, respectively. Thereby, $\mathrm{ESR}_{C_{s1}}$ and $\mathrm{ESR}_{C_{s2}}$ are the equivalent series resistance of the SCC, while $R_{ds,on}$ symbolizes the MOSFETs' equivalent on-resistance. Moreover, the coefficients A and B are defined in (19) and (20), respectively. In the case that $\mathrm{ESR}_{C_{s2}}$ is similar to $R_{ds,on}$, the equivalent resistance of the SCC would be approximately constant over x. Otherwise, the SCC

resistance would vary with similar trend to Fig. 8. The step-by-step computation of (17) and (18) is explained in Appendix B

$$R_{f-w} = A\left(2x + \frac{\sin \pi (1-2x)}{\pi}\right) + \mathrm{ESR}_{C_{s2}} + \mathrm{ESR}_{C_{s1}} \quad (17)$$

$$R_{h-w} = B\left(2x - \frac{\sin 4\pi x}{2\pi}\right) + \mathrm{ESR}_{C_{s2}} + \mathrm{ESR}_{C_{s1}} \quad (18)$$

$$A = R_{\mathrm{ds,ON}(S_1)} + R_{\mathrm{ds,ON}(S_2)} - \mathrm{ESR}_{C_{s2}} \quad (19)$$

$$B = R_{\mathrm{ds,ON}(S_3)} - \mathrm{ESR}_{C_{s2}}. \quad (20)$$

C. Design Guideline for EV Wireless Charging Systems

The requirements for the design of an EV wireless charging system that operates with the proposed COL method are as follows:

1) the range of V_{batt} during one complete charging cycle;
2) the maximum $P_{\mathrm{grid,max}}$ that can be drawn from the grid;
3) the range of V_{in} available from the PFC;
4) the maximum voltage stress $\hat{V}_{C_{s2}}$ allowed by the semiconductor switches of the SCCs.

The battery voltage V_{batt} varies while its SoC increases. For instance, V_{batt} ranges from a minimum $V_{\mathrm{batt,min}}$ to a maximum $V_{\mathrm{batt,max}}$. These values are intrinsic of each EV battery.

Assuming that the input reactive power is negligible, the maximum input active power $P_{\mathrm{grid,max}}$ depends on the selected SAE J2954 power class, here being 3.7 kW (WPT1).

When considering the input to be connected to one phase of the European 50-Hz grid, the phase-to-neutral voltage is 230-V rms with a tolerance of $\pm 10\%$. Thus, the available range of V_{in} from a boost-like single-phase PFC is >358 V.

At this point, given the range of V_{batt}, $P_{\mathrm{grid,max}}$, V_{in}, and a preliminary-conservative efficiency η^* assumption, e.g., 92%, measured between the 50-Hz ac connection and the EV battery, the maximum deliverable output current $I_{\mathrm{out,max}}$ can be calculated through (21). The latter considers that $V_{\mathrm{out}} = V_{\mathrm{batt}}$, as shown in Fig. 2(c). During one battery charging cycle, $I_{\mathrm{out}} = I_{\mathrm{out,max}}$ corresponds to the maximum power point of the COL profile, which has been marked with five-pointed stars in Fig. 3(b)

$$I_{\mathrm{out,max}} = \frac{P_{\mathrm{grid,max}} \cdot \eta^*}{V_{\mathrm{out,max}}}. \quad (21)$$

The primary and secondary resonant circuits are designed to satisfy all conditions in (22).

From the first condition in (22), the ratio (R_1/R_2) is calculated, such that V_{in} and V_{out} are within the given ranges. After that, the span of M from which it is possible to keep $R_{L,\mathrm{opt}}$ constant is computed by solving the second condition of (22), where $I_{\mathrm{out,max}}$ is given in (21). For instance, $M_{\max}$ is found for $\omega_0 = \omega_{0,\min} = 2\pi \cdot 79$ kHz, while $M_{\min}$ is found for $\omega_0 = \omega_{0,\max} = 2\pi \cdot 90$ kHz. This target range of M can result from any arrangement of coupled coils. However, the value of L_1, L_2, and k in the third condition must be selected, such that the peak voltage stress on the SCC's MOSFET is within the rating of the selected semiconductor switch. This is discussed more in detail in Section III-D

$$\begin{cases} (7) = \dfrac{V_{\mathrm{out,max}}}{R_{L,\mathrm{opt}}} \rightarrow \sqrt{\dfrac{R_1}{R_2}} = \dfrac{V_{\mathrm{in,max}}}{V_{\mathrm{out,max}}} \\ R_{L,\mathrm{opt}} = \dfrac{V_{\mathrm{out,max}}}{I_{\mathrm{out,max}}} \rightarrow M = \dfrac{8}{\pi^2}\dfrac{1}{\omega_0}\dfrac{V_{\mathrm{out,max}}}{I_{\mathrm{out,max}}}\sqrt{\dfrac{R_1}{R_2}} \quad \text{where:} \\ \omega_0 = 2\pi\,[79, \ldots, 90]\ \mathrm{kHz} \\ Q_1 = \dfrac{\omega_0 L_1}{R_1},\ Q_2 = \dfrac{\omega_0 L_2}{R_2} \rightarrow \dfrac{L_1}{L_2} = \dfrac{Q_1}{Q_2}\left(\dfrac{V_{\mathrm{in,max}}}{V_{\mathrm{out,max}}}\right)^2 \\ kL_1L_2 = M \rightarrow (14) : \hat{V}_{C_{s2,1}}, \hat{V}_{C_{s2,2}} < V_{\mathrm{ds,off}(S_5/S_6)}. \end{cases} \quad (22)$$

D. Prototype of 3.7-kW EV Wireless Charging System

The guideline of Section III-C has resulted in the circuit parameters and components summarized in Table I.

1) Variable Compensation Capacitors C_1, C_2: To achieve the COL operation at different coil's alignments, f_0 of the IPT system must be varied, as shown in Fig. 5. The value of the passive components must be chosen, such that the voltage stress over the SCC's MOSFETs is within its rated value including a safe margin to account for dynamic operating conditions.

Fig. 9 shows the examples of the voltage stress and the values of L_1, L_2, C_{s1}, and C_{s2} depending on k for different power levels. The design guidelines in (22) have been used assuming that $Q_1 = Q_2$. The peak voltage on C_{s2} has been computed through (23) and (24) for the two modulations where the primary and secondary currents are calculated through (25). Since 1700-V SiC MOSFETs are used in the SCCs, the conservative maximum voltage stress of 1 kV is selected in Fig. 9 for the steady-state operation to ensure enough safety margin also when transients occur

$$\hat{V}_{C_{s2},f-w} = \int_{x\frac{T}{2}+\frac{T}{4}}^{\frac{T}{2}} \frac{\hat{I}_{C_{s1}}}{C_{s2}} \sin \omega t dt = \frac{\hat{I}_{C_{s1}}}{\omega C_{s2}}\left[1 + \cos \pi \left(\frac{1}{2} + x\right)\right] \quad (23)$$

$$\hat{V}_{C_{s2},h-w} = \int_{xT}^{\frac{T}{2}} \frac{\hat{I}_{C_{s1}}}{C_{s2}} \sin \omega t dt = \frac{\hat{I}_{C_{s1}}}{\omega C_{s2}}(1 + \cos 2\pi x) \quad (24)$$

$$\hat{I}_1 \approx \left|\frac{4}{\pi} I_{\mathrm{out}} \frac{R_{L,\mathrm{opt}}}{\omega_{0,\max} M_{\min}}\right|, \quad \hat{I}_2 \approx \frac{\pi}{2} I_{\mathrm{out}}. \quad (25)$$

The values of C_{s1} and C_{s2} have been chosen, such that the f_0 variation in the range $70, \ldots, 90$ kHz is achievable given L_1 and L_2, and considering that x is fully utilized. For instance, if L is the coils' inductance, the minimum and maximum needed capacitance can be found from (12) as

$$C_{\min} = \frac{1}{\left(\omega_{0,\max} L - X\right) \cdot \omega_{0,\max}}$$

$$C_{\max} = \frac{1}{\left(\omega_{0,\min} L - X\right) \cdot \omega_{0,\min}}. \quad (26)$$

Then, C_{s1} and C_{s2} are computed as

$$C_{s1} = C_{\max}, \quad C_{s2} = \frac{C_{\max} \cdot C_{\min}}{C_{\max} - C_{\min}}. \quad (27)$$

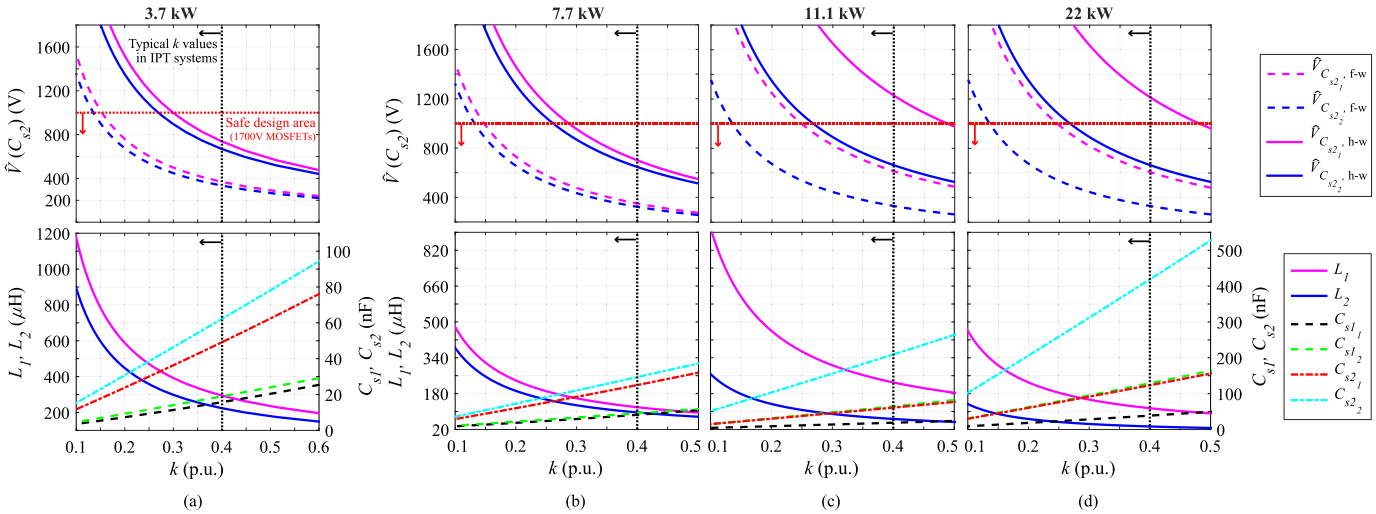

Fig. 9. Voltage stress across the SCC's MOSFETs, values of L_1, L_2, C_{s1}, and C_{s2} depending on k at different power levels. (a) 3.7 kW ($I_{\text{batt}} = 7.48$ A, $M_{\text{min}} = 90.1$ μH). (b) 7.7 kW ($I_{\text{batt}} = 17$ A, $M_{\text{min}} = 37.6$ μH). (c) 11.1 kW ($I_{\text{batt}} = 25$ A, $M_{\text{min}} = 43.6$ μH). (d) 22 kW ($I_{\text{batt}} = 50$ A, $M_{\text{min}} = 21.8$ μH).

TABLE I

CIRCUIT PARAMETERS AND COMPONENTS USED IN THE PROPOSED 3.7-kW EV WIRELESS CHARGING SYSTEM IN FIG. 10

Circuit parameters					**Component**	**Function**	**Units**	**Manufacturer**	**Name**
f (kHz)	[79 90]		**Primary**	**Secondary**	1200V SiC MOSFET	Inverter	4	Wolfspeed	C2M0040120D
$P_{\text{grid,max}}$ (kW)	3.7	C_{s1_1}, C_{s1_2} (nF)	13.50	18.57	1200V SiC diode	Rectifier	4		C4D15120D
η^* (%)	92	C_{s2_1}, C_{s2_2} (nF)	28.03	52.08	1700V SiC MOSFET	SCC **	1/2x2		C2M0045170P
V_{in}(V)	[358 510]	L_1, L_2 (µH)	336.90	224.15	6.8 nF 500 V_{rms}	C_{s1_1}	11x4	EPCOS	B32671L
V_{batt}(V)	[317 410]	R_{L_1}, R_{L_2} (Ω)	0.75	0.5		C_{s2_1}	6x3		
$R_{L,opt}$ (Ω)	54.8	M (µH)	[102.6	95.4 90.1]		C_{s1_2}	16x4		
Z_{ag} (mm)	105		[M_{max}	M_{mid} M_{min}]		C_{s2_2}	11x3		
Misalignment [(x,y,z) mm]		$M_{\text{max}} \rightarrow$ (0, 0, Z_{ag}) $M_{\text{mid}} \rightarrow$ [(67, 0, Z_{ag}) or (0, 37, Z_{ag})] $M_{\text{min}} \rightarrow$ [(82, 0, Z_{ag}) or (0, 45, Z_{ag})]				C_1^{***}	9x4		
						C_2^{***}	11x4		
					** h-w/f-w, *** fixed S-S: C_1/C_2=(15.14/18.55)(nF)				
Measuring and supplying equipment		Oscilloscope: YOKOGAWA DLM4058 2.5GS/s 500MHz Power analyzer: YOKOGAWA WT500 Bidirectional DC power supplies: DELTA ELEKTRONIKA SM1500-CP-30 (input), SM500-CP-90 (output)							

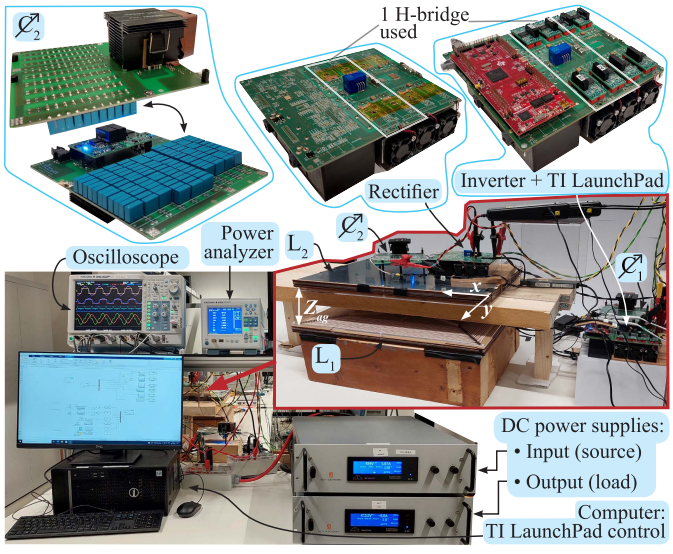

Fig. 10. Prototype of the 3.7-kW EV wireless charging system.

Based on the resulting voltage stress in Fig. 9, it is possible to employ SCCs with both modulations for the power levels of 3.7 and 7.7 kW. On the other hand, that might not be the case of the two highest power levels. In general, the full-wave modulation comprehends a wider range of coils' arrangements that would ensure an SCC's voltage stress within the safe area. In particular, if the coupled coils have relatively high k, e.g., $k \approx 0.4$, it might be possible to employ 1200-V SiC MOSFETs for SCCs using the full-wave modulation. The advantages of this choice are discussed in Section IV-A.

According to the implemented 3.7-kW prototype shown in Fig. 10, the resulting variations of C_1 and C_2 are illustrated in Fig. 11(a) and (b) by using SCCs with full-wave modulation and half-wave modulation, respectively. Thereby, C_1 and C_2 follow the trend described by (15) and (16), which depends on SCC's duty cycle $x = (t_{\text{ON}}/T) = [0, \ldots, 0.5]$. The validity of these analytical expressions has been proven by measuring the circuit's resonant frequency at different values of x. To prevent the coils' mutual inductance from altering this calculation, the measurements have been executed considering the primary and the secondary circuits separately. Assuming that L_1 and L_2 are known, one can compute the equivalent compensation capacitance from (4) by imposing $X_1 = X_2 = 0$.

2) Control Scheme for V_{in} and $f_0(C_1, C_2)$: The detailed control scheme is summarized in Fig. 12. There are two sets of parameters to be regulated in the proposed system. One is the duty cycle of the PFC rectifier D_{PFC} that sets the target V_{in}. The other is the duty cycle of both SCCs, namely, x_1 and x_2,

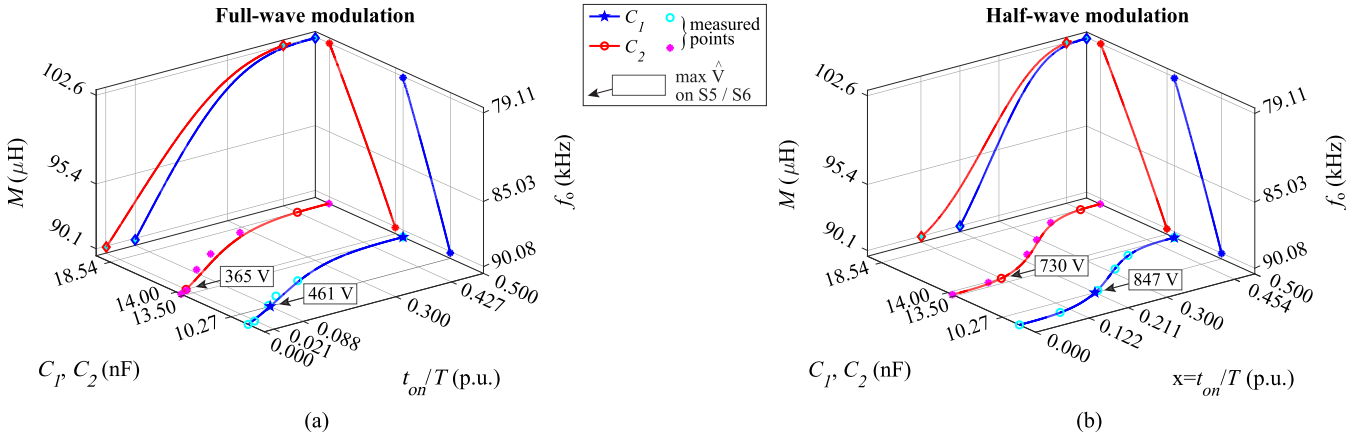

Fig. 11. Values of C_1 and C_2 using the SCCs with (a) full-wave and (b) half-wave modulations. Note that the standardized operating frequency range 79–90 kHz established by IPT-based EV charging is satisfied in the current system design.

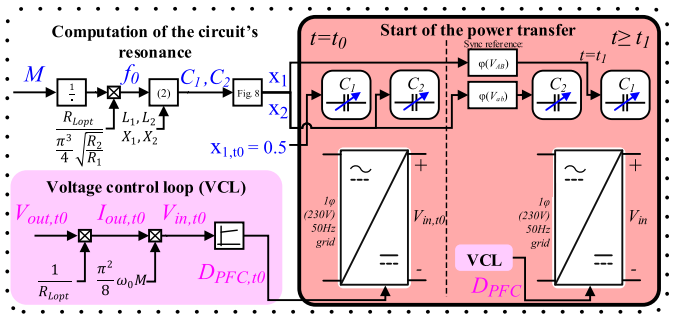

Fig. 12. Detailed control scheme referring to the charging process in Fig. 6. In the prototype of Fig. 10, the operation of the PFC rectifier is modeled by the input dc power supply.

establishing the IPT system's resonant frequency f_0. In the prototype of Fig. 10, the input voltage V_{in} is regulated by a dc power supply, which resembles the voltage range that the PFC rectifier could provide. This is reasonable, since the PFC rectifier is a necessary power conversion stage for any EV wireless charging system, given that they are commonly connected to the ac grid. In addition, the battery behavior is emulated by a bidirectional dc power supply.

Before the start of the power transfer, the values of x_1, x_2, and $D_{\text{PFC},t0}$ are computed based on the measurements of M, $V_{\text{out},t0}$ and the reference R_{Lopt}.

When the power transfer starts at the instant $t = t_0$, the operating frequency of the inverter is set to the target f_0, and the input voltage would be $V_{\text{in},t0}$. However, at that instant of time, the duty cycle of the primary SCC assumes the initial value $x_{1,t0} = 0.5$ while $x_{2,t0} = x_2$. This results in the operation being in the inductive region of the resonant circuit, since C_1 assumes its highest value, which translates into a safe operation for the H-bridge inverter. At the instant $t = t_1$, x_1 is set for the primary SCC, whose control signal is synchronized to the output voltage from the H-bridge inverter V_{AB}. On the other hand, the control signal of the secondary SCC is synchronized with respect to the rectifying H-bridge's input voltage V_{ab}. Assuming that, from (8)–(11), the phase delay of both the primary and the secondary currents is known, a phase shift can be set to x_1 and x_2, making sure that they are synchronized with the resonant currents, resulting in the ZVS of the SCCs. Measurements based on this proposed startup scheme can be found in Section IV-A.

For the rest of the charging process ($t > t_1$), the same SCC control signals apply. Therefore, the SCC signals must be adjusted only at the beginning of the charging process. On the other hand, D_{PFC} starts from the initial value $D_{\text{PFC},t0}$, and it is continuously modified by the voltage control loop to achieve the COL charging mode in Fig. 3(b).

IV. Experimental Results

A. COL Method With SCCs

1) Measured Circuit Waveforms: Fig. 13(a) and (b) shows the measured waveforms of the proposed COL method at different values of M defined in Table I. Two sets of measurements have been executed to compare the performance of the two possible SCC implementations illustrated in Fig. 7. For instance, the measurements in Fig. 13(a) have been performed while employing SCCs with full-wave modulation. On the other hand, the measurements in Fig. 13(b) use SCCs with half-wave modulation. As expected, the resonant circuit's input and output waveforms from the two implementations are equivalent for the same operating conditions. The main difference between the two implementations is the voltage $v_{C_{s2}}$ due to the different modulation strategies. As a result, the voltage stress on the MOSFETs of the SCCs with half-wave modulation is about twice the voltage stress of each MOSFET employed in the full-wave modulation. The measured peaks of $\hat{V}_{C_{s2,1}}$ and $\hat{V}_{C_{s2,2}}$ agree with the expected values from the analytical model shown in Fig. 11.

The startup transient following the control strategy illustrated in Fig. 12 has been measured at $V_{\text{batt}} = 317$ V, as shown in Figs. 14 and 15 for the full-wave and half-wave modulations, respectively. This operation occurs if the charging cycle starts when the battery's SoC = 0%. Moreover, Figs. 16 and 17 show the startup transient measured at full power ($V_{\text{batt}} = 410$ V) for both modulations. All these measurements have been executed at $M = M_{\text{min}}$, since it leads to the highest voltage stress on the SCCs' MOSFETs. It is possible to notice that the ZVS turn-on of the H-bridge is maintained during the whole transient, since i_1 is always

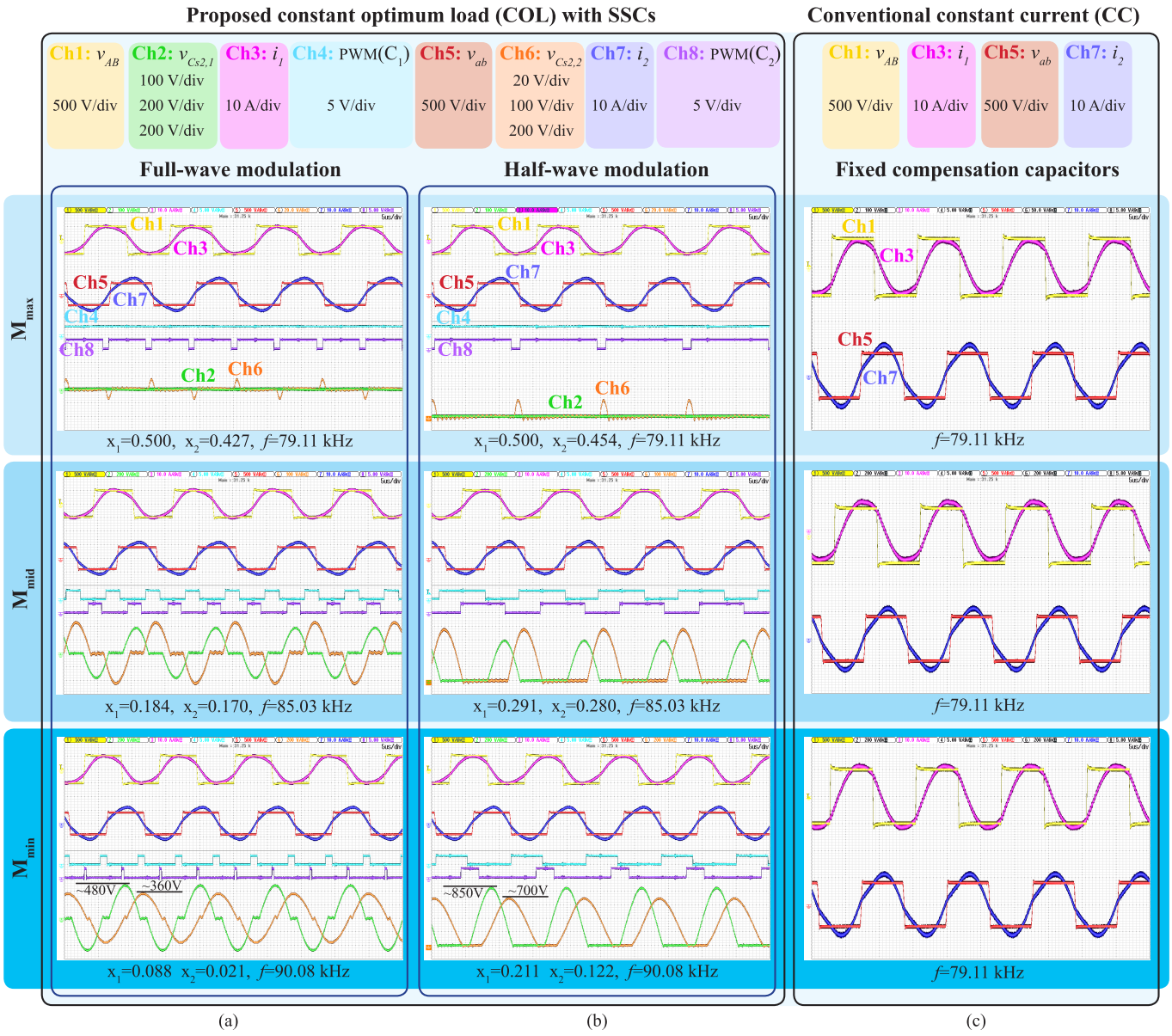

Fig. 13. Waveforms measured at full power and at different coils' alignments. (a) and (b) Result from the proposed COL using the SCCs with the full-wave and half-wave modulations, respectively. (c) Results from the conventional S–S compensation with fixed capacitors.

inductive. The SCC MOSFETs' peak voltage stress is well below 1700 V. At $V_{\text{batt}} = 410$ V, the worst measured voltage stress is $\hat{V}_{C_{s2},1} = 1000$ V using the full-wave modulation, and $\hat{V}_{C_{s2},1} = 1450$ V for the half-wave modulation.

According to Fig. 13, the SCCs introduce some distortion in the currents. This is particularly clear when employing the half-wave modulation where the positive and the negative currents' half waves are not symmetrical. This is due to the asymmetrical nature of the half-wave modulation that foresees the switching only in correspondence of one zero crossing during one switching period. Nevertheless, the ZVS turn-on operation can be observed by analyzing the H-bridge inverter output voltage in Fig. 13, which has a smooth (dv/dt) transition, i.e., without abrupt variations. The asymmetry in the primary current would cause the H-bridge inverter's turn-off point to slightly vary in the two switching transitions. This is shown in Fig. 18 where the drain–source voltage v_{ds} of both MOSFETs $M1$ and $M3$ in Fig. 2(c) is measured at $M = M_{\text{mid}}$ and $M = M_{\text{min}}$. The ZVS turn-on is achieved, since the $(\text{d}v/\text{d}t)$ is smooth and the primary current lags that transition.

2) Power Transfer Efficiency: The dc-to-dc efficiency η of these two implementations is illustrated in Fig. 19 in relation to a charging profile similar to the one in Fig. 3(b). The implementation of SCCs with half-wave modulation leads to higher efficiency. mainly because it employs two less SiC MOSFETs than the full-wave modulation, resulting in lower conduction losses. The switching losses are also lower, since the SCC is switched on and off only once every switching cycle, while these transitions occur twice in the full-wave modulation. For instance, the measured η at the maximum P_{in} (around 3.2 kW) is 96.30% for $M = M_{\text{max}}$, and 96.07%

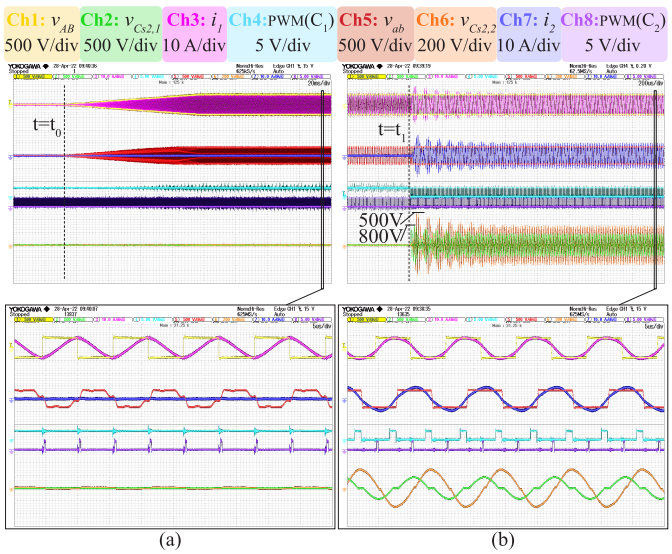

Fig. 14. Start of the power transfer with SCCs using the full-wave modulation at $M = M_{\text{min}}$ and $V_{\text{batt}} = 317$ V, referring to Fig. 12. (a) At $t = t_0$, $V_{\text{in},t0}$ is applied while $x_{1,t0} = 0.5$ and $x_2 = 0.021$. (b) At $t = t_1$, $x_1 = 0.088$ is applied. The channels are displayed in the same sequence of Fig. 13.

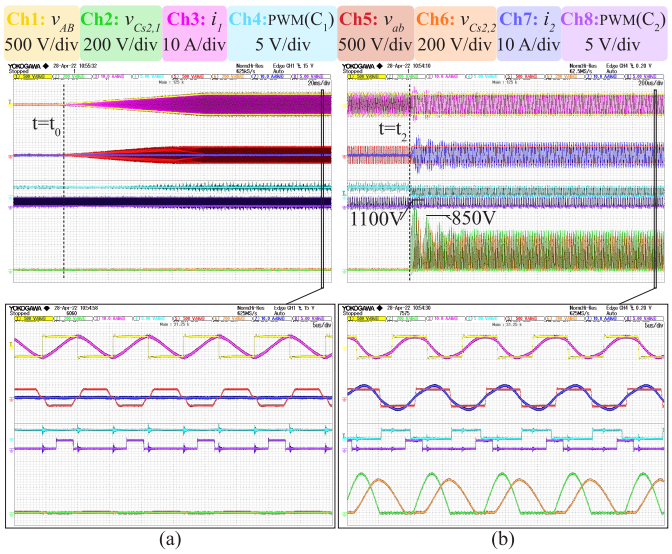

Fig. 15. Start of the power transfer with SCCs using the half-wave modulation at $M = M_{\text{min}}$ and $V_{\text{batt}} = 317$ V referring to Fig. 12. (a) At $t = t_0$, $V_{\text{in},t0}$ is applied while $x_{1,t0} = 0.5$ and $x_2 = 0.122$. (b) At $t = t_1$, $x_1 = 0.211$ is applied. The channels are displayed in the same sequence of Fig. 13.

for $M = M_{\text{min}}$ when using the half-wave modulation. For the same operating points, the measured η values are 96.18% and 95.76% in the case of the full-wave modulation. However, the latter has margin still for improvement.

According to the startup transient in Fig. 16, the peak voltage stress on the SCC's MOSFETs is 1000 V when using the full-wave modulation. This means that 1200-V SiC MOSFETs could be employed in that case. The main advantages of these devices are their larger market availability and their lower $R_{\text{ds,on}}$ for the same current rating due to their thinner epitaxial layer. Table II shows that, at full power when $M = M_{\text{max}}$, the SCC using the full-wave modulation employing 1200-V SiC MOSFETs could outperform the efficiency measured with the half-wave modulation for a lower total semiconductor's cost

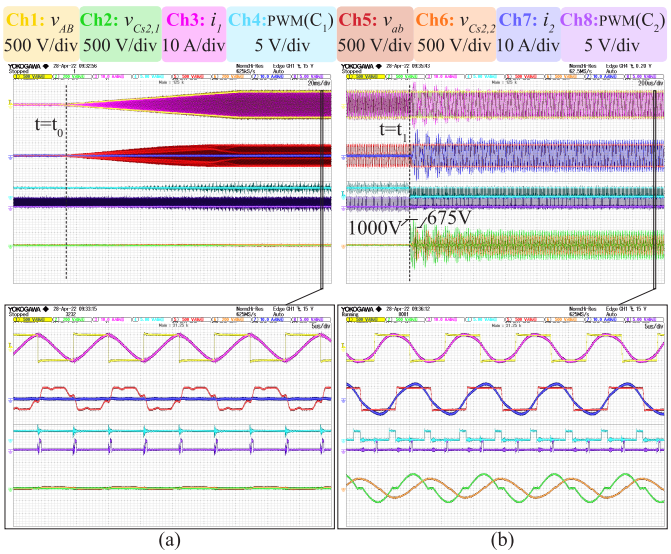

Fig. 16. Start of the power transfer with SCCs using the full-wave modulation at $M = M_{\text{min}}$ and $V_{\text{batt}} = 410$ V, referring to Fig. 12. (a) At $t = t_0$, $V_{\text{in},t0}$ is applied while $x_{1,t0} = 0.5$ and $x_2 = 0.021$. (b) At $t = t_1$, $x_1 = 0.088$ is applied. The channels are displayed in the same sequence of Fig. 13.

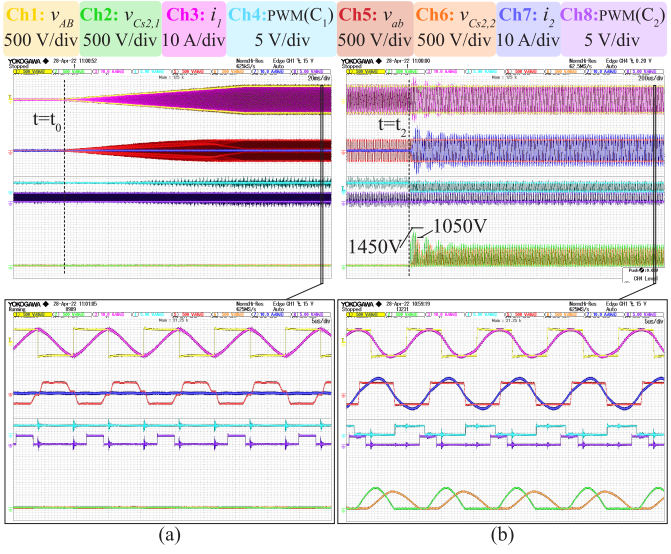

Fig. 17. Start of the power transfer with SCCs using the half-wave modulation at $M = M_{\text{min}}$ and $V_{\text{batt}} = 410$ V referring to Fig. 12. (a) At $t = t_0$, $V_{\text{in},t0}$ is applied while $x_{1,t0} = 0.5$ and $x_2 = 0.122$. (b) At $t = t_1$, $x_1 = 0.211$ is applied. The channels are displayed in the same sequence of Fig. 13.

TABLE II

WOLFSPEED SiC MOSFETs CHARACTERISTICS AND COMPUTED η WHEN EMPLOYING THEM FOR SCCs WITH FULL-WAVE MODULATION

SiC MOSFET	V_{ds} (V)	$R_{ds,on}$ (mΩ)	Cost (€)*	η (%)**
C2M0045170P	1700	45	75.85	96.18
C3M0032120K	1200	32	24.39	96.32
C3M0021120K	1200	21	28.43	96.41
C3M0016120K	1200	16	66.92	96.45

*Source: Digi-key Electronics (accessed: 03/05/2022). Unit price (100+)
**Computed at full power, i.e., V_{batt}=410 V and M=M_{max}

(approximately −25%). On the other hand, according to the peak voltage stress in Fig. 17, it is not possible with the current design to choose MOSFETs with lower voltage rating in the case of SCCs with the half-wave modulation.

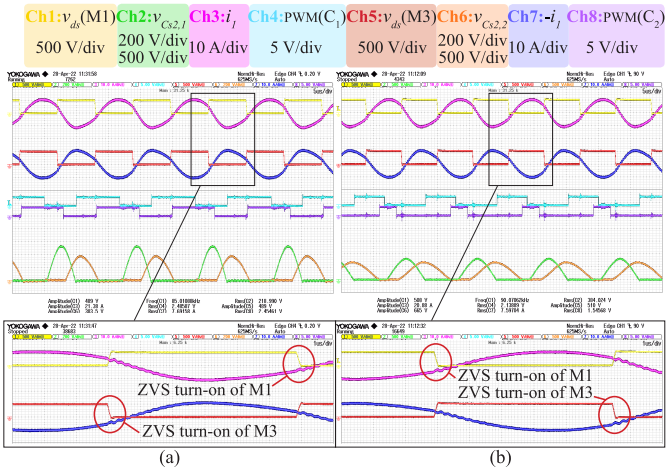

Fig. 18. Measured drain–source voltage $v_{\rm ds}$ of the MOSFETs $M1$ and $M3$ in Fig. 2 when operating the SCCs with the half-wave modulation at full power for (a) $M = M_{\rm mid}$ and (b) $M = M_{\rm min}$. The channels are displayed in the same sequence of Fig. 13.

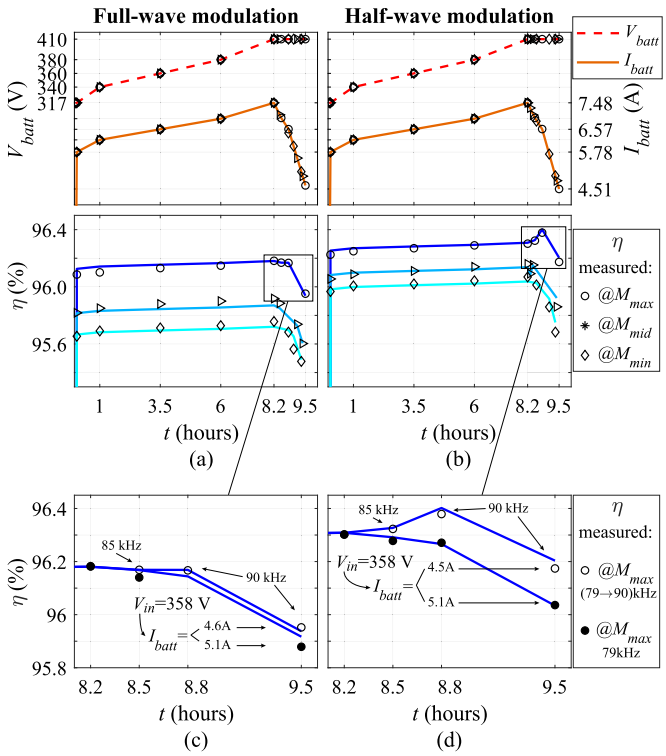

Fig. 19. Measured dc-to-dc efficiency η at different M values of the proposed COL charging method that uses SCCs as compensation implemented with (a) full-wave and (b) half-wave modulations. (c) and (d) Possibility of improving η and reaching lower $I_{\rm batt}$ at partial load by varying f_0 and setting $f = f_0$. The continuous lines are the expected results from the analytical model.

As explained in Section II-B2, the CV charging profile can be achieved by controlling the input voltage through the PFC. The CV mode is characterized by a charging current lower than the nominal, i.e., $R_L > R_{L,\rm opt}$. By considering the definition of $R_{L,\rm opt}$ in (6), the system's natural frequency f_0 can be varied through the SCCs, such that $R_{L,\rm opt}$ is closer to R_L at partial loads. This can potentially increase the efficiency at partial load. Moreover, according to $I_{\rm out}$ in (2), the increase of f_0 would also allow the CV mode to reach lower currents for

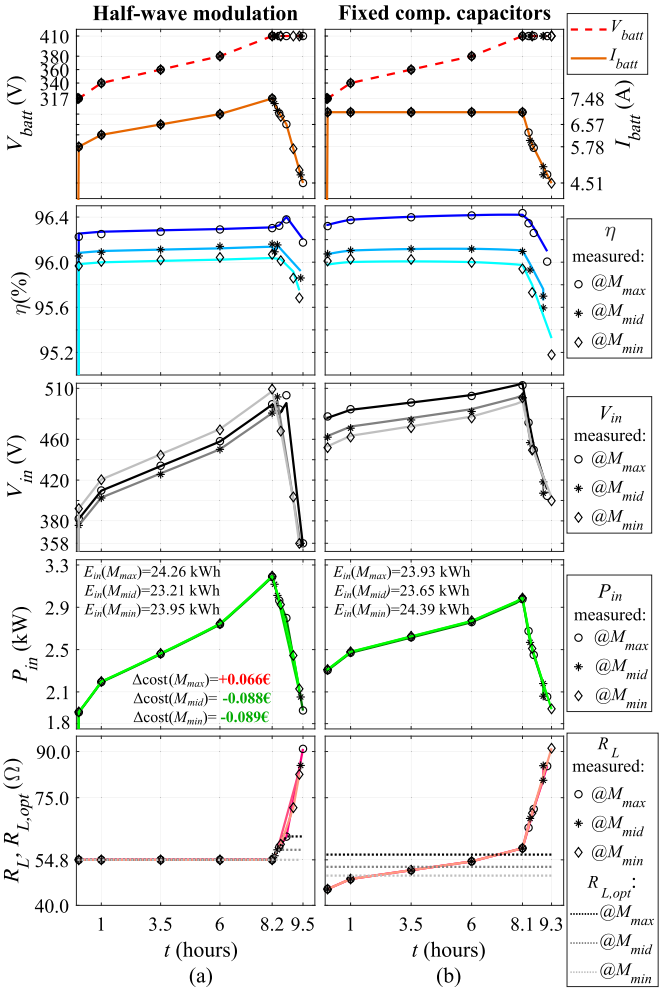

Fig. 20. Measured dc-to-dc efficiency η, input voltage $V_{\rm in}$, input power $P_{\rm in}$, equivalent resistive load R_L, and optimum load $R_{L,\rm opt}$ achieved from (a) proposed COL method implemented with SCCs using half-wave modulation and (b) traditional CC method employing fixed capacitors. The continuous lines are the expected results from the analytical model.

the same $V_{\rm in}$. The effect of this partial-load strategy is shown in Fig. 19(c) and (d) for $M = M_{\rm max}$, where both the resonant and operating frequency are increased from 79 to 90 kHz. Thereby, η improvement is up to 0.13% for the half-wave modulation and up to 0.07% for the full-wave modulation. On top of this, about 10% lower output current can be achieved for the same input voltage.

B. Comparison With the Conventional S–S Compensation

To investigate further the advantages of the proposed COL method, it is important to compare its performance with conventional CC changing mode implemented with an S–S compensation with fixed capacitance. The parameters of the latter are listed in Table I. C_1 has been chosen, such that the inverter achieves the ZVS turn-on at 79 kHz in any operating condition, and the output power can be controlled through the full voltage range available from the PFC stage. The operating waveforms at full power and at different coils' alignments are shown in Fig. 13(c).

The measured dc-to-dc efficiency η, the set input voltage $V_{\rm in}$ and power $P_{\rm in}$, the equivalent resistive load R_L, and the

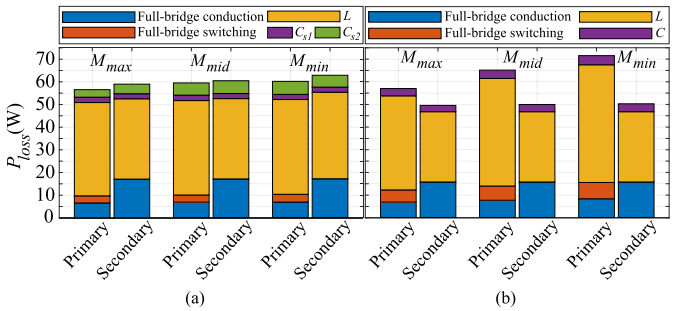

Fig. 21. Breakdown of the power losses at full power resulting from (a) proposed COL method with SCCs using half-wave modulation and (b) traditional CC method employing fixed compensation capacitors. The coils' and capacitors' losses include also the losses due to cables and connections.

optimum load $R_{L,\text{opt}}$ of these two different implementations are illustrated in Fig. 20 in relation to a charging profile similar to the one of the Nissan Leaf's battery in Fig. 3.

The implementation of SCCs with half-wave modulation leads to 0.13% lower η at $M = M_{\max}$ than the conventional S–S compensation throughout the COL charging profile mainly because of conduction losses due to the SCC extra series capacitor in parallel with the SiC MOSFET. This can be noticed in the losses breakdown of Fig. 21. On the other hand, in the presence of coils' misalignment, the half-wave modulation leads to higher η, since the condition $R_L = R_{L,\text{opt}}$ is kept constant. According to Fig. 20, this drop in η when using fixed capacitors occurs at partial load and lower magnetic coupling. This happens because, in that cases, the condition $R_L = R_{L,\text{opt}}$ is poorly matched, which results in an imbalanced distribution of the power losses between the primary and the secondary circuits shown in Fig. 21. In addition, from the power losses' distribution in Fig. 21(a), it is clear that the amount of circulating reactive current with the proposed method is approximately constant at different coils' alignments, which limits the turn-off losses of the H-bridge inverter. These features are not found in the conventional S–S compensation, resulting in higher losses in the primary circuit, as shown in Fig. 21(b). As depicted in the plot of P_{in}, higher η results in lower required input energy $E_{\text{in}} = P_{\text{in}} \cdot t$ by up to $\Delta E_{\text{in}} = 440$ Wh, which translated into lower charging cost even though the charging duration is slightly higher due to the variable I_{batt} characteristic of the proposed COL method.

The measurements of V_{in} show that it is possible to follow the battery charging profile in both implementations by only regulating the power through the PFC stage. It is also interesting to notice that the S–S compensation with fixed capacitors could reach lower I_{batt} values in the CV mode, since V_{in} still has a margin to be lowered to 358 V. However, only the values of I_{batt} that are comparable to the ones achieved with the half-wave modulation have been reported in Fig. 20 for being able to compare fairly the two CV modes.

In addition, the overall efficiency could be considerably improved if SiC MOSFETs were used in the rectification stage instead of diodes. For example, using the same SiC MOSFETs as the inverter, the measured full-power efficiency of 96.30% could improve to 96.77% when employing SCCs with half-wave modulation at $M = M_{\max}$. Similarly, at $M = M_{\min}$, the full-power efficiency could jump to 96.5% from the measured 96.07%. In this case, the proposed method would result in even higher efficiency than the available in the literature for the same power level (see Fig. 1).

V. Conclusion

The optimum load matching is widely used in EV wireless charging systems, where the equivalent output load is always set to equal the so-called optimum load. The latter maximizes the power transfer efficiency, and its value is dependent on the coils' alignment. In contrast, this article proposed to make the optimum load condition invariant of the coil's magnetic coupling by changing the natural resonant frequency of the system. This method is defined here as COL. The advantage of this solution is the elimination of voltage control at the load side. Only the input power is regulated through the PFC, ensuring that the COL condition is met while the battery voltage increases during the charging cycle. The system's resonant frequency is varied, employing SCCs as series compensation. In particular, two SCC implementations, namely, the full-wave modulation and the half-wave modulation, have been implemented in a 3.7-kW prototype, and their performances have been compared. The half-wave modulation results in overall higher efficiency than full-wave modulation, with 96.30% for the input power of 3.2 kW and at the maximum coils' alignment. For the same power and minimum alignment, the efficiency drops only by 0.27%. The minimum measured efficiency is 95.68% at partial load and minimum coupling, proving that the proposed method leads to relatively high efficiency in the entire operating range. On the other hand, at 3.2 kW and the maximum magnetic coupling, the full-wave modulation results in 96.18%, and the efficiency drops by 0.42% at the minimum alignment. When misalignment occurs, the SCC half-wave modulation is more efficient than the conventional S–S compensation with fixed capacitors. The efficiency gain is up to 0.68% at partial load. Finally, considering the high power transfer efficiency measured for a coil's misalignment range and throughout a charging cycle typical of a 3.7-kW static EV wireless charger, this research has proved the suitability of the proposed COL charging method for that application.

Appendix A
Step-by-Step Computation of (10)

The instantaneous primary current can be expressed as

$$i_1(t) = \hat{I}_1 \sin(\omega t - \theta_1) \tag{28}$$

where θ_1 is the phase delay with respect to the inverted voltage v_{AB}. The value of θ_1 that corresponds to the optimized ZVS turn-on point can be found from (28) by setting $i_1(\text{T}) = I_{\text{OFF}}$

$$I_{\text{OFF}} = \hat{I}_1 \sin(\pi - \theta_1) \quad \rightarrow \quad \theta_1 = \sin^{-1}\left(\frac{I_{\text{OFF}}}{\hat{I}_1}\right). \tag{29}$$

The phase angle of the input impedance $\boldsymbol{Z}_{\text{in}} = (\boldsymbol{V_{AB}}/\boldsymbol{I_{AB}})$ would also be θ_1. According to $\boldsymbol{Z}_{\text{in}}$ in (11), this means that

$$\theta_1 = \tan\left(\frac{X_{\text{in}}}{R_{\text{in}}}\right) = \tan\left(\frac{X_1}{R_{\text{in}}}\right). \tag{30}$$

The reactance X_1 that leads to the optimized ZVS turn-on operation can be found from (29) and (30) resulting in (10).

The expression of X_2 in (8) has been found with a similar approach by taking the load impedance as a reference.

APPENDIX B
STEP-BY-STEP COMPUTATION OF (17) AND (18)

The conduction losses of the two SCC implementations shown in Fig. 7 are given by the rms current that flows in each parallel branch of the SCC, which depends on the SCC duty cycle $x = (t_{\mathrm{ON}}/T) = [0, \ldots, 0.5]$. During one switching period T, the current of the SCC series capacitor $i_{C_{s1}}$ flows through the semiconductor branch of the SCC for the interval $2\mathrm{x}T$, while it flows through C_{s2} for $(1-2x)T$. The resulting rms current of each SCC parallel branch is shown in (31) and (32) for the full-wave and half-wave modulations, respectively. As expected, these expressions are the functions of $\hat{I}_{C_{s1}}$ and x

$$f-w: \begin{cases} I_{C_{s2}} = \hat{I}_{C_{s1}} \sqrt{\left(\frac{1}{2}-x\right) - \frac{\sin\left(\pi\left(1-2x\right)\right)}{2\pi}} \\ I_{S_1\&S_2} = \hat{I}_{C_{s1}} \sqrt{x + \frac{\sin\left(\pi\left(1-2x\right)\right)}{2\pi}} \end{cases} \tag{31}$$

$$h-w: \begin{cases} I_{C_{s2}} = \hat{I}_{C_{s1}} \sqrt{\left(\frac{1}{2}-x\right) + \frac{\sin\left(4\pi x\right)}{4\pi}} \\ I_{S_3} = \hat{I}_{C_{s1}} \sqrt{x - \frac{\sin\left(4\pi x\right)}{4\pi}}. \end{cases} \tag{32}$$

After that, the conduction loss of the SCC can be calculated, as shown in (33) and (34). From those, the equivalent resistance of the SCC can be computed by isolating $I_{C_{s1}}$, whose R_{f-w} results in (17) and R_{h-w} in (18)

$$\begin{aligned} P_{\mathrm{SCC}(f-w)} &= \mathrm{ESR}_{C_{s2}} I_{C_{s2}}^2 + \left(R_{\mathrm{ds,ON}(S_1)} + R_{\mathrm{ds,ON}(S_2)}\right) I_{S_1\&S_2}^2 \\ &= R_{f-w} I_{C_{s1}}^2 \end{aligned} \tag{33}$$

$$\begin{aligned} P_{\mathrm{SCC}(h-w)} &= \mathrm{ESR}_{C_{s2}} I_{C_{s2}}^2 + R_{\mathrm{ds,ON}(S_3)} I_{S_3}^2 \\ &= R_{h-w} I_{C_{s1}}^2. \end{aligned} \tag{34}$$

REFERENCES

[1] J. Andersson, M. Nilsson, and S. Pettersson, "Introducing wireless charging for drivers of electrical vehicles in Sweden—Effects on charging behaviour and attitudes," in *Advances in Human Aspects of Transportation*. Cham, Switzerland: Springer, 2017, pp. 951–962.

[2] S. Li and C. C. Mi, "Wireless power transfer for electric vehicle applications," *IEEE J. Emerg. Sel. Topics Power Electron.*, vol. 3, no. 1, pp. 4–17, Mar. 2015.

[3] V. Cirimele, M. Diana, F. Freschi, and M. Mitolo, "Inductive power transfer for automotive applications: State-of-the-art and future trends," *IEEE Trans. Ind. Appl.*, vol. 54, pp. 4069–4079, Sep./Oct. 2018.

[4] H. Feng, R. Tavakoli, O. C. Onar, and Z. Pantic, "Advances in high-power wireless charging systems: Overview and design considerations," *IEEE Trans. Transport. Electrific.*, vol. 6, no. 3, pp. 886–919, Sep. 2020.

[5] *Wireless Power Transfer for Light-Duty Plug-in/Electric Vehicles and Alignment Methodology*, document J2954 (R), SAE International, Oct. 2020.

[6] R. Bosshard, J. W. Kolar, J. Mühlethaler, I. Stevanović, B. Wunsch, and F. Canales, "Modeling and η-α-Pareto optimization of inductive power transfer coils for electric vehicles," *IEEE J. Emerg. Sel. Topics Power Electron.*, vol. 3, no. 1, pp. 50–64, Mar. 2015.

[7] R. Bosshard and J. W. Kolar, "Multi-objective optimization of 50 kW/85 kHz IPT system for public transport," *IEEE J. Emerg. Sel. Topics Power Electron.*, vol. 4, no. 4, pp. 1370–1382, Dec. 2016.

[8] M. Lu and K. D. T. Ngo, "A fast method to optimize efficiency and stray magnetic field for inductive-power-transfer coils using lumped-loops model," *IEEE Trans. Power Electron.*, vol. 33, no. 4, pp. 3065–3075, Apr. 2018.

[9] S. Bandyopadhyay, P. Venugopal, J. Dong, and P. Bauer, "Comparison of magnetic couplers for IPT-based EV charging using multi-objective optimization," *IEEE Trans. Veh. Technol.*, vol. 68, no. 6, pp. 5416–5429, Jun. 2019.

[10] W. Shi, F. Grazian, S. Bandyopadhyay, J. Dong, T. B. Soeiro, and P. Bauer, "Analysis of dynamic charging performances of optimized inductive power transfer couplers," in *Proc. IEEE 19th Int. Power Electron. Motion Control Conf. (PEMC)*, Apr. 2021, pp. 751–756.

[11] B.-G. Choi and Y.-S. Kim, "New structure design of ferrite cores for wireless electric vehicle charging by machine learning," *IEEE Trans. Ind. Electron.*, vol. 68, no. 12, pp. 12162–12172, Dec. 2021.

[12] M. Xiong, X. Wei, Y. Huang, Z. Luo, and H. Dai, "Research on novel flexible high-saturation nanocrystalline cores for wireless charging systems of electric vehicles," *IEEE Trans. Ind. Electron.*, vol. 68, no. 9, pp. 8310–8320, Sep. 2021.

[13] Y. Jiang, L. Wang, J. Fang, R. Li, R. Han, and Y. Wang, "A high-efficiency ZVS wireless power transfer system for electric vehicle charging WithVariable angle phase shift control," *IEEE J. Emerg. Sel. Topics Power Electron.*, vol. 9, no. 2, pp. 2356–2372, Apr. 2021.

[14] R. Bosshard, J. W. Kolar, and B. Wunsch, "Control method for inductive power transfer with high partial-load efficiency and resonance tracking," in *Proc. Int. Power Electron. Conf. (IPEC-Hiroshima ECCE ASIA)*, May 2014, pp. 2167–2174.

[15] H. Li, J. Li, K. Wang, W. Chen, and X. Yang, "A maximum efficiency point tracking control scheme for wireless power transfer systems using magnetic resonant coupling," *IEEE Trans. Power Electron.*, vol. 30, no. 7, pp. 3998–4008, Jul. 2015.

[16] T. Diekhans and R. W. D. Doncker, "A dual-side controlled inductive power transfer system optimized for large coupling factor variations and partial load," *IEEE Trans. Power Electron.*, vol. 30, no. 11, pp. 6320–6328, Nov. 2015.

[17] W. X. Zhong and S. Y. R. Hui, "Maximum energy efficiency tracking for wireless power transfer systems," *IEEE Trans. Power Electron.*, vol. 30, no. 7, pp. 4025–4034, Jul. 2015.

[18] T.-D. Yeo, D. Kwon, S.-T. Khang, and J.-W. Yu, "Design of maximum efficiency tracking control scheme for closed-loop wireless power charging system employing series resonant tank," *IEEE Trans. Power Electron.*, vol. 32, no. 1, pp. 471–478, Jan. 2017.

[19] R. Bosshard and J. W. Kolar, "All-SiC 9.5 kW/dm^3 on-board power electronics for 50 kW/85 kHz automotive IPT system," *IEEE J. Emerg. Sel. Topics Power Electron.*, vol. 5, no. 1, pp. 419–431, Mar. 2017.

[20] R. Mai, Y. Liu, Y. Li, P. Yue, G. Cao, and Z. He, "An active-rectifier-based maximum efficiency tracking method using an additional measurement coil for wireless power transfer," *IEEE Trans. Power Electron.*, vol. 33, no. 1, pp. 716–728, Jan. 2018.

[21] J. Zhang, J. Zhao, Y. Zhang, and F. Deng, "A wireless power transfer system with dual switch-controlled capacitors for efficiency optimization," *IEEE Trans. Power Electron.*, vol. 35, no. 6, pp. 6091–6101, Jun. 2020.

[22] Z. Huang, C.-S. Lam, P.-I. Mak, R. P. D. S. Martins, S.-C. Wong, and C. K. Tse, "A single-stage inductive-power-transfer converter for constant-power and maximum-efficiency battery charging," *IEEE Trans. Power Electron.*, vol. 35, no. 9, pp. 8973–8984, Sep. 2020.

[23] J. Osawa, T. Isobe, and H. Tadano, "Efficiency improvement of high frequency inverter for wireless power transfer system using a series reactive power compensator," in *Proc. IEEE 12th Int. Conf. Power Electron. Drive Syst. (PEDS)*, Dec. 2017, pp. 992–998.

[24] D. Kim and D. Ahn, "Self-tuning LCC inverter using PWM-controlled switched capacitor for inductive wireless power transfer," *IEEE Trans. Ind. Electron.*, vol. 66, no. 5, pp. 3983–3992, May 2018.

[25] J. Zhao, J. Zhang, Y. Zhang, Z. Din, and J. Juri, "A reactive compensation method using switch controlled capacitor for wireless power transfer," in *Proc. IEEE Energy Convers. Congr. Expo. (ECCE)*, Sep. 2019, pp. 2112–2117.

[26] W. Li, G. Wei, C. Cui, X. Zhang, and Q. Zhang, "A double-side self-tuning LCC/S system using a variable switched capacitor based on parameter recognition," *IEEE Trans. Ind. Electron.*, vol. 68, no. 4, pp. 3069–3078, Apr. 2021.

[27] J. Wang, Z. Chang, B. Zhang, X. Yang, and H. Tang, "Analysis of ICPT system with LCC resonant topology based on the switch-controlled capacitor," in *Proc. IEEE Wireless Power Transf. Conf. (WPTC)*, Nov. 2020, pp. 178–182.

[28] S. Lu, T. Lammle, and N. Parspour, "Analysis and design of a T-compensation network with switch-controlled capacitor for wireless power transfer system," in *Proc. IEEE PELS Workshop Emerg. Technol., Wireless Power Transf. (WoW)*, Jun. 2021, pp. 1–6.
[29] X. Wang, J. Xu, M. Leng, H. Ma, and S. He, "A hybrid control strategy of LCC-S compensated WPT system for wide output voltage and ZVS range with minimized reactive current," *IEEE Trans. Ind. Electron.*, vol. 68, no. 9, pp. 7908–7920, Sep. 2021.
[30] M. Schweizer and T. B. Soeiro, "Heatsink-less quasi 3-level flying capacitor inverter based on low voltage SMD MOSFETs," in *Proc. 19th Eur. Conf. Power Electron. Appl. (EPE ECCE Eur.)*, Sep. 2017, p. 10.
[31] F. Grazian, W. Shi, T. B. Soeiro, J. Dong, and P. Bauer, "Electric vehicle charging based on inductive power transfer employing variable compensation capacitance for optimum load matching," in *Proc. IECON 46th Annu. Conf. IEEE Ind. Electron. Soc.*, Oct. 2020, pp. 5262–5267.
[32] Z. Qingwei, W. Lifang, and L. Chenglin, "Compensate capacitor optimization for kilowatt-level magnetically resonant wireless charging system," *IEEE Trans. Ind. Electron.*, vol. 61, no. 12, pp. 6758–6768, Dec. 2014.
[33] T. Kan, T.-D. Nguyen, J. C. White, R. K. Malhan, and C. C. Mi, "A new integration method for an electric vehicle wireless charging system using LCC compensation topology: Analysis and design," *IEEE Trans. Power Electron.*, vol. 32, no. 2, pp. 1638–1650, Feb. 2017.
[34] L. Zhao, D. Thrimawithana, and U. K. Madawala, "Hybrid bidirectional wireless EV charging system tolerant to pad misalignment," *IEEE Trans. Ind. Electron.*, vol. 64, no. 9, pp. 7079–7086, Sep. 2017.
[35] K. Inoue, K. Kusaka, and J.-I. Itoh, "Reduction in radiation noise level for inductive power transfer systems using spread spectrum techniques," *IEEE Trans. Power Electron.*, vol. 33, no. 4, pp. 3076–3085, Apr. 2018.
[36] J. Lu, G. Zhu, D. Lin, S.-C. Wong, and J. Jiang, "Load-independent voltage and current transfer characteristics of high-order resonant network in IPT system," *IEEE J. Emerg. Sel. Topics Power Electron.*, vol. 7, no. 1, pp. 422–436, Mar. 2019.
[37] L. Zhao, D. J. Thrimawithana, U. K. Madawala, A. P. Hu, and C. C. Mi, "A misalignment-tolerant series-hybrid wireless EV charging system with integrated magnetics," *IEEE Trans. Power Electron.*, vol. 34, no. 2, pp. 1276–1285, Feb. 2018.
[38] Z. Zhang, F. Zhu, D. Xu, P. T. Krein, and H. Ma, "An integrated inductive power transfer system design with a variable inductor for misalignment tolerance and battery charging applications," *IEEE Trans. Power Electron.*, vol. 35, no. 11, pp. 11544–11556, Nov. 2020.
[39] L. Zhao, D. J. Thrimawithana, U. K. Madawala, and A. P. Hu, "A push–pull parallel resonant converter-based bidirectional IPT system," *IEEE Trans. Power Electron.*, vol. 35, no. 3, pp. 2659–2667, Mar. 2020.
[40] X. Zhang, Y. Zhang, Z. Zhang, and M. Li, "Mode conversion and structure optimization of quadrature coils for electric vehicles wireless power transfer," *IEEE Trans. Energy Convers.*, vol. 35, no. 2, pp. 575–590, Jun. 2020.
[41] C. Xiao, B. Cao, and C. Liao, "A fast construction method of resonance compensation network for electric vehicle wireless charging system," *IEEE Trans. Instrum. Meas.*, vol. 70, pp. 1–9, 2021.
[42] R. L. Steigerwald, "A comparison of half-bridge resonant converter topologies," *IEEE Trans. Power Electron.*, vol. PE-3, no. 2, pp. 174–182, Apr. 1988.
[43] T. B. Soeiro and P. Bauer, "Fast DC-type electric vehicle charger based on a quasi-direct boost–buck rectifier," in *Proc. AEIT Int. Conf. Electr. Electron. Technol. Automot. (AEIT AUTOMOTIVE)*, Jul. 2019, pp. 1–6.
[44] *Electric Vehicle Wireless Power Transfer (WPT) Systems—Part 1: General Requirements*, Standard IEC 61980-1:2020, International Electrotechnical Commissio, Nov. 2020.
[45] F. Grazian, P. van Duijsen, T. B. Soeiro, and P. Bauer, "Advantages and tuning of zero voltage switching in a wireless power transfer system," in *Proc. IEEE PELS Workshop Emerg. Technol., Wireless Power Transf. (WoW)*, Jun. 2019, pp. 367–372.
[46] J. Kolar, J. Biela, and J. Minibock, "Exploring the Pareto front of multi-objective single-phase PFC rectifier design optimization–99.2% efficiency vs. 7kW/din^3 power density," in *Proc. IEEE 6th Int. Power Electron. Motion Control Conf.*, May 2009, pp. 1–21.
[47] M. S. Ortmann, T. B. Soeiro, and M. L. Heldwein, "High switches utilization single-phase PWM boost-type PFC rectifier topologies multiplying the switching frequency," *IEEE Trans. Power Electron.*, vol. 29, no. 11, pp. 5749–5760, Nov. 2014.
[48] W. J. Gu and K. Harada, "A new method to regulate resonant converters," *IEEE Trans. Power Electron.*, vol. PE-3, no. 4, pp. 430–439, Oct. 1988.

Francesca Grazian (Graduate Student Member, IEEE) received the bachelor's degree in electrical engineering from the University of Bologna, Bologna, Italy, in 2016, and the master's degree in electrical engineering from the Delft University of Technology, Delft, The Netherlands, in 2018, with a focus on power electronics, where she is currently pursuing the Ph.D. degree.

Her research interest includes wireless power transfer.

Prof. Grazian was a recipient of the Best Poster Award in the 2022 European Ph.D. School sponsored by the European Center of Power Electronics (ECPE).

Thiago Batista Soeiro (Senior Member, IEEE) received the B.Sc. (Hons.) and M.Sc. degrees in electrical engineering from the Federal University of Santa Catarina, Florianópolis, Brazil, in 2004 and 2007, respectively, and the Ph.D. degree from the Swiss Federal Institute of Technology, Zürich, Switzerland, in 2012.

He was a Visiting Scholar with the Power Electronics and Energy Research Group, Concordia University, Montreal, QC, Canada, and the Center for Power Electronics Systems, Blacksburg, VA, USA. From 2012 to 2013, he was a Researcher with the Power Electronics Institute, Federal University of Santa Catarina. From 2013 to 2018, he was a Senior Scientist with the Corporate Research Center, ABB Switzerland Ltd., Baden, Switzerland. From 2018 to 2022, he has been with the DC Systems, Energy Conversion and Storage Group, Delft University of Technology, Delft, The Netherlands, as an Associate Professor. Since 2022, he has been with the Power Management and Distribution Section (TEC-EPM), European Space Research and Technology Centre, Noordwijk, The Netherlands. His research interests include advanced high power converters and dc system integration.

Dr. Soeiro was a recipient of the 2013 IEEE Industrial Electronics Society Best Conference Paper Award and the Best Paper Awards in the following IEEE conferences: International Conference on Power Electronics (ECCE Asia 2011), International Conference on Industrial Technology (ICIT 2013), and Conference on Power Electronics and Applications EPE'15 (ECCE Europe 2015).

Pavol Bauer (Senior Member, IEEE) received the master's degree in electrical engineering from the Technical University of Kosice, Kosice, Slovakia, in 1985, and the Ph.D. degree from the Delft University of Technology, Delft, The Netherlands, in 1995.

He was on many projects for industry concerning wind and wave energy, power electronic applications for power systems, such as Smarttrafo; HVdc systems, projects for smart cities, such as photovoltaic (PV) charging of electric vehicles, PV and storage integration, contactless charging; and he participated in several Leonardo da Vinci and H2020 EU projects as a Project Partner (ELINA, INETELE, and E-Pragmatic) and a Coordinator (PEMCWebLab.com-Edipe, SustEner, and Eranet DCMICRO). He has authored or coauthored eight books, holds four international patents, and organized several tutorials at the international conferences. He is currently a Full Professor with the Department of Electrical Sustainable Energy, Delft University of Technology, and the Head of the DC Systems, Energy Conversion and Storage Group.

Prof. Bauer is a member of the Executive Committee of European Power Electronics Association and the International Steering Committee at numerous conferences. He is the Former Chairman of the Benelux IEEE Joint Industry Applications Society and the Power Electronics and Power Engineering Society Chapter. He is the Chairman of the Power Electronics and Motion Control Council.